AGU PUBLICATIONS

Space Weather

RESEARCH ARTICLE
10.1002/2015SW001174

Key Points:
- Performance metrics for solar wind simulation are developed
- Ten model combinations are validated with strengths and weaknesses diagnosed
- Stream interactions are captured 30–80% of the time and by 0.5–2.5 days off

Supporting Information:
- Supporting Information S1

Correspondence to:
L. K. Jian,
lan.jian@nasa.gov

Citation:
Jian, L. K., P. J. MacNeice, A. Taktakishvili, D. Odstrcil, B. Jackson, H.-S. Yu, P. Riley, I. V. Sokolov, and R. M. Evans (2015), Validation for solar wind prediction at Earth: Comparison of coronal and heliospheric models installed at the CCMC, *Space Weather*, *13*, 316–338, doi:10.1002/2015SW001174.

Received 4 FEB 2015
Accepted 11 APR 2015
Accepted article online 16 APR 2015
Published online 27 MAY 2015

Validation for solar wind prediction at Earth: Comparison of coronal and heliospheric models installed at the CCMC

L. K. Jian[1,2], P. J. MacNeice[2], A. Taktakishvili[2,3], D. Odstrcil[2,4], B. Jackson[5], H.-S. Yu[5], P. Riley[6], I. V. Sokolov[7], and R. M. Evans[4]

[1]Department of Astronomy, University of Maryland, College Park, Maryland, USA, [2]Heliophysics Science Division, NASA Goddard Space Flight Center, Greenbelt, Maryland, USA, [3]Department of Physics, Catholic University of America, Washington, District of Columbia, USA, [4]School of Physics, Astronomy, and Computational Sciences, George Mason University, Fairfax, Virginia, USA, [5]Center for Astrophysics and Space Sciences, University of California, San Diego, La Jolla, California, USA, [6]Predictive Science Inc., San Diego, California, USA, [7]Department of Atmospheric, Oceanic, and Space Sciences, University of Michigan, Ann Arbor, Michigan, USA

Abstract Multiple coronal and heliospheric models have been recently upgraded at the Community Coordinated Modeling Center (CCMC), including the Wang-Sheeley-Arge (WSA)-Enlil model, MHD-Around-a-Sphere (MAS)-Enlil model, Space Weather Modeling Framework (SWMF), and heliospheric tomography using interplanetary scintillation data. To investigate the effects of photospheric magnetograms from different sources, different coronal models, and different model versions on the model performance, we run these models in 10 combinations. Choosing seven Carrington rotations in 2007 as the time window, we compare the modeling results with the Operating Mission as Nodes on the Internet data for near-Earth space environment during the late declining phase of solar cycle 23. Visual comparison is proved to be a necessary addition to the quantitative assessment of the models' capabilities in reproducing the time series and statistics of solar wind parameters. The MAS-Enlil model captures the time patterns of solar wind parameters better, while the WSA-Enlil model matches with the time series of normalized solar wind parameters better. Models generally overestimate slow wind temperature and underestimate fast wind temperature and magnetic field. Using improved algorithms, we have identified magnetic field sector boundaries (SBs) and slow-to-fast stream interaction regions (SIRs) as focused structures. The success rate of capturing them and the time offset vary largely with models. For this quiet period, the new version of MAS-Enlil model works best for SBs, while heliospheric tomography works best for SIRs. The new version of SWMF with more physics added needs more development. General strengths and weaknesses for each model are diagnosed to provide an unbiased reference to model developers and users.

1. Motivation

We are motivated to validate the coronal and heliospheric models for the quasi-steady solar wind from the following three respects. First, a stream interaction region (SIR) forms when fast wind overtakes and interacts with the proceeding slow wind. It is in nature the same as the commonly known corotating interaction region [e.g., *Smith and Wolfe*, 1976; *Gosling and Pizzo*, 1999]. However, we use SIRs to emphasize that when the solar background changes within one Carrington rotation (CR), the resultant SIRs are short lived and do not corotate with the Sun to recur. In fact, *Jian et al.* [2006, 2011a] find 51% of SIRs near solar maximum and 10% at solar minimum do not recur at Earth. Large-amplitude Alfvén waves [*Belcher and Davis*, 1971] in SIRs and the following fast wind can drive a series of particle injections and affect the evolution of outer radiation belt (centered at about 4 R_E), as demonstrated in *Miyoshi and Kataoka* [2005]. Additionally, in geomagnetic storms, a large amount of energy is transferred from the solar wind into the magnetosphere and eventually dissipated in the thermosphere (about 90–600 km aboveground) and ionosphere (about 60–1000 km aboveground) by Joule heating and auroral precipitation [e.g., *Gonzalez et al.*, 1994, and references therein]. The energy dissipation in the thermosphere can trigger variations of thermospheric densities, which can further perturb the orbits for low Earth orbit (LEO) satellites and space stations [e.g., *Wilson et al.*, 2006; *Anderson et al.*, 2009; *Xu et al.*, 2011]. Because SIR-driven geomagnetic storms last longer than the ones driven by coronal mass ejections (CMEs), they have a larger effect on the total orbital decay of LEO satellites and space stations [e.g., *Chen et al.*, 2014]. Thus, space weather forecasting includes the prediction of SIR arrival.

Second, Earth's magnetosphere and ionosphere respond differently to different orientations of the interplanetary magnetic field (IMF) [e.g., *Heppner*, 1972; *Russell and McPherron*, 1973; *Brecht et al*., 1981; *Fedder et al*., 1995]. Although the north-south IMF component (B_z) is crucial for geomagnetic activity, it varies frequently nearly randomly in the background solar wind. Even though there may be methods for postprocessing model data to statistically include such field fluctuation, it is hard for models to produce the realistic magnetic field out of the ecliptic plane, not to mention predict the right B_z magnitude. Correct prediction of the field polarity in the ecliptic plane is the first step toward capturing the full IMF vector. In addition, the different orientations of the IMF in the ecliptic plane can have different geoeffect [e.g., *Brecht et al*., 1981] and even affect the atmospheric escape rates at Venus differently [e.g., *Collinson et al*., 2015]. Thus, herein we assess how well the models can capture the inward/outward polarity of the IMF. It can measure the quality of the models' reproduction of the overall magnetic configurations and the resultant sector boundaries (SBs) between the magnetic Northern (outward) and Southern (inward) Hemispheres [*MacNeice*, 2009a]. Note SBs and heliospheric current sheets are treated as the same concept herein.

Third, CMEs as the major driver of space weather are frequently launched in or near the coronal streamer belt [e.g., *Hundhausen*, 1993; *Crooker et al*., 1998], and they need to propagate through the medium of a structured ambient solar wind. The SIRs and IMF SBs can affect the propagation of CMEs and possibly distort the flux-rope topology often embedded within CMEs [e.g., *Odstrčil and Pizzo*, 1999a, 1999b; *Vandas and Odstrčil*, 2000; *Case et al*., 2008; *Gopalswamy et al*., 2009; *Manchester et al*., 2014]. In addition, the accurate representation of ambient solar wind is related to getting the right shock parameters, which are input for solar energetic particle (SEP) acceleration models. Hence, the successful prediction of background solar wind is needed for predicting CMEs and SEPs as well and has become a part of space weather forecasting [e.g., *Zheng et al*., 2013].

2. Introduction

The Community Coordinated Modeling Center (CCMC, see http://ccmc.gsfc.nasa.gov/) is a multiagency partnership located at the NASA Goddard Space Flight Center (GSFC) to enable, support, and perform the research and development for next generation space science and space weather models. More than 10 coronal and heliospheric models are installed at the CCMC, most of which are available for run request. Among them, the following models are widely used to generate the background plasma and/or magnetic field condition in the corona and/or inner heliosphere: Wang-Sheeley-Arge (WSA) model, MHD-Around-a-Sphere (MAS) model, Enlil model, Space Weather Modeling Framework (SWMF), and heliospheric tomography. This work validates these models and helps them get ready for the transition from research to operation.

The WSA model includes solar coronal (SC) and inner heliospheric (IH) components. The coronal part combines a Potential-Field Source Surface (PFSS) model [*Altschuler and Newkirk*, 1969; *Schatten et al*., 1969] with the Schatten current sheet model [*Schatten*, 1971] to produce a global magnetic field configuration at 21.5 solar radii (R_υ), while using an improved Wang and Sheeley empirical relationship [*Wang and Sheeley*, 1990a, 1990b, 1992; *Arge and Pizzo*, 2000; *Arge et al*., 2002] to derive the solar wind speed at 21.5 R_υ. Based on the assumption of constant mass flux and speed-temperature relation in *Lopez* [1987], the WSA model also derives the density and temperature kinematically in heliosphere [e.g., *Owens et al*., 2005]. A new Air Force Data Assimilative Photospheric Flux Transport (ADAPT) model [*Arge et al*., 2010, 2011] including the farside observation of active regions [*Arge et al*., 2013] is in development and not yet available at the CCMC at this writing.

The MAS model is a three-dimensional (3-D) time-dependent model built on the resistive MHD equations and developed by the Predictive Science [e.g., *Mikić and Linker*, 1994, 1996; *Linker et al*., 1996, 2003; *Riley et al*., 2001a, 2001b]. It has SC (1–30 R_υ) and IH (outer boundary at 1.1 AU at CCMC) parts as well. The MAS coronal model first uses a potential field model and a Parker solar wind solution to determine the initial plasma and magnetic field parameters then solves the Maxwell equations and the continuity, momentum, and energy equations to get a steady state MHD solution. We run the coupled MAS coronal and Enlil heliospheric models in the corona-heliosphere (CORHEL) module at CCMC, because the MAS IH part installed at CCMC cannot provide results at Ulysses orbit which is needed for an accompanying study. Two versions of the CORHEL are compared in this study: v4.7 and v5.0. Both of these versions support the MAS model with a polytropic form of the energy equation. They also include some ad hoc corrections at 30 R_υ for solar wind speed based on the expected velocity dependence on the distance of field line photospheric foot points from the closest coronal hole boundary [*Riley et al*., 2001a, 2001b]. The CORHEL v5.0, available since

April 2014, includes an additional version of MAS model which supports a full thermodynamic energy equation [*Lionello et al*., 2009], and we include it in the evaluation.

The Enlil model is a 3-D time-dependent heliospheric model based on the ideal MHD equations developed by Dusan Odstrcil and his colleagues. The inner boundary of Enlil model is placed at 21.5 or 30 R_υ beyond the outermost critical point and the outer boundary is 2 AU in our runs and adjustable to 5 or 10 AU [e.g., *Odstrčil*, 1994; *Odstrčil et al*., 1996; *Odstrčil and Pizzo*, 1999a]. At the inner boundary, the solar rotation is added by imparting a corotational magnetic field component. Without artificial diffusion, the Enlil model produces second-order accuracy while providing the stability that ensures nonoscillatory solutions [*Odstrcil*, 2003]. It implements a dimensional splitting technique for computational efficiency [*Odstrcil*, 2003]. In recent years, the Enlil model coupled with WSA or MAS coronal model has been widely used [e.g., *Odstrcil et al*., 2002, 2004; *Riley et al*., 2002]. In particular, the Enlil model coupled with the WSA coronal model is currently used in operational space weather forecasting at NOAA [*Pizzo et al*., 2011]. However, since the installation of this new version 2.7 at the CCMC in May 2011, it has not been extensively validated by third party except for case studies, e.g., in *Jian et al*. [2011b]. The previous version of Enlil uses free magnetic field strength at the inner boundary and only tracks the location of the sector boundaries. In contrast, the new version uses the changing magnetic field provided by the coronal models, which is ultimately based on synoptic maps; therefore, it has better tracing of the IMF than before [*Jian et al*., 2011b]. In addition, Enlil version 2.7 fixes the spiral shape problem in previous versions by setting the azimuthal field dependent on the local solar wind speed from coronal model rather than that assuming the solar wind is fast everywhere [*Jian et al*., 2011b].

The SWMF is a well-coupled modeling system developed by the Center for Space Environment Modeling team at the University of Michigan [e.g., *Tóth et al*., 2005, 2012]. We only use its SC (1–24 R_υ) and IH (24–500 R_υ) components. Both components are based on the Block-Adaptive Tree Solarwind Roe-type Upwind Scheme code that can solve various forms of the MHD equations [*Powell et al*., 1999; *Gombosi et al*., 2001, 2004]. We compare two recent versions of SWMF in this study. The earlier v8.03 was installed at the CCMC in January 2012. It set an inner boundary in the 1 MK corona, had separate electron and ion temperatures, and incorporated the collisional electron heat conduction as well as Alfvén wave transport and dissipation along the open field lines [*van der Holst et al*., 2010]. *Sokolov et al*. [2013] improved the two-temperature model by incorporating MHD Alfvén wave turbulence in a semiempirical heating model and putting balanced turbulence at the apex of the closed field lines. This model can resolve the upper chromosphere and transition region besides the corona. Based on it, *van der Holst et al*. [2014] added anisotropic ion temperature and Alfvén wave reflection and built the Alfvén Wave Solar Model (AWSoM) without relying on any ad hoc heating function. This model is the SC and IH components of the present v9.20 of SWMF, and it became available at CCMC in May 2014.

The heliospheric tomography is a 3-D reconstruction technique incorporating a kinematic solar wind model and tomographically fitting it to remotely sensed observations of the solar wind. There are two versions of this technique at the CCMC, developed by the Center for Astrophysics and Space Sciences at the University of California, San Diego (UCSD) [e.g., *Jackson et al*., 1997, 1998, 2011]. One version uses interplanetary scintillation (IPS) data [e.g., *Hewish et al*., 1964; *Coles*, 1978; *Manoharan et al*., 1995; *Manoharan*, 2010; *Tokumaru*, 2013]. One existing IPS system that provides IPS data continually throughout the year from radio telescopes is operated by the Solar Terrestrial Environment Laboratory at Nagoya University in Japan [e.g., *Tokumaru et al*., 2011]. Scintillation-level intensity is related to the small-scale interplanetary density variations along the lines of sight to point radio sources [*Hewish et al*., 1964]. Analyses of these remotely sensed solar wind data can provide solar wind densities and bulk speeds. The other version of the heliospheric tomography uses the observation of white light Thomson scattering brightness from the Solar Mass Ejection Imager [e.g., *Eyles et al*., 2003; *Jackson et al*., 2004], available for years 2003–2010. We choose the CCMC tomography version using IPS data for this validation because IPS arrays are still in operation, and there are several IPS arrays around the globe, some of which are upgraded or newly built [e.g., *Swarup et al*., 1971; *González-Esparza et al*., 2006; *van Haarlem et al*., 2013].

The SC parts of the WSA, MAS, and SWMF models all use full-rotation synoptic magnetograms as inner boundary condition at the CCMC, and the full-rotation maps are constructed from a CR sequence of (usually) daily full-disk photospheric magnetograms [*Arge and Pizzo*, 2000]. All these models accept

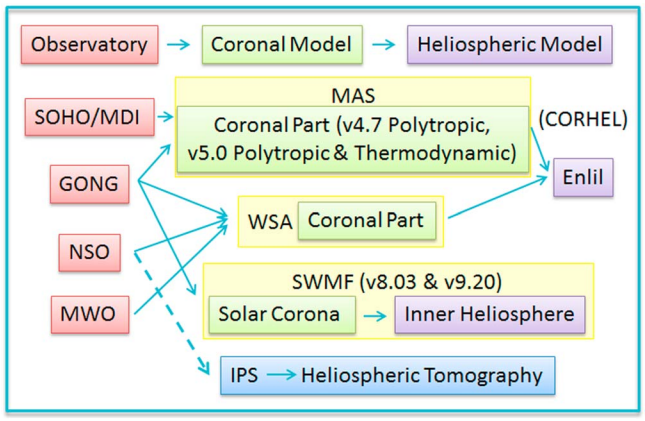

Figure 1. The coupling of synoptic magnetograms, coronal models, and heliospheric models to be validated in this study. See text and supporting information Table S1 for denotations of acronyms. Two versions of MAS model and SWMF are indicated.

the magnetograms from the Global Oscillation Network Group (GONG) consisting of six stations worldwide [*Harvey et al.*, 1996]. In addition, the WSA model takes the magnetograms from the Mount Wilson Observatory (MWO) [*Ulrich et al.*, 2002] and the National Solar Observatory (NSO) at Kitt Peak in Arizona [*Pierce*, 1969], while the MAS model takes the input from NSO and the Michelson Doppler Imager (MDI) [*Scherrer et al.*, 1995] on board the Solar and Heliospheric Observatory (SOHO). Currently, the WSA and MAS models also claim to accept user-supplied synoptic maps but not any other type of user-supplied coronal boundary condition.

At CCMC, the WSA/MAS-Enlil model and SWMF IH part provide the solar wind plasma and IMF output at the trajectories of planets and major spacecraft within 2 AU per request, including Mercury, Venus, Earth, the Mercury Surface, Space Environment, Geochemistry, and Ranging spacecraft; Solar Terrestrial Relations Observatory A/B; and Ulysses. One can also plot and/or download the 3-D plasma and magnetic field data in the SC and IH regions additional to the above selected locations. For IPS tomography, the output at these selected planets and spacecraft has not yet been made available in a digital format at CCMC except for the movies of solar wind density and velocity at Earth, so the timeline data are provided directly by the UCSD group. In addition, the UCSD group can provide the radial and tangential IMF components, which is not available at the CCMC site. First, the daily updated NSO magnetogram data are interpreted using the Current-Sheet Source Surface (CSSS) model developed by *Zhao and Hoeksema* [1995] that extrapolates the data to 15 R_s. Second, the UCSD group uses a 2-D spline fit interpolation of such magnetic field data to obtain regular inputs at the same time cadence at which the tomography is run. It is possible for them to use magnetograms from GONG or other sources in the future.

In addition to the validation from each modeling team, there are many third party validation efforts for quasi-steady solar wind excluding CMEs [e.g., *Owens et al.*, 2005, 2008; *Lee et al.*, 2009; *MacNeice*, 2009a, 2009b; *Jian et al.*, 2011b]. However, there is not sufficient intercomparison between different models. Model developers and users do not always know the strengths and weaknesses of each model. This study fills this gap and also updates the validation with the model upgrades using modified metrics. Herein, we validate the following models as shown in Figure 1: (1) the WSA coronal part + Enlil model (in short, WSA-Enlil), (2) the MAS coronal part + Enlil model (in short, MAS-Enlil), (3) the SWMF, and (4) the heliospheric tomography using IPS data and convecting outward the magnetic field from NSO (in short, NSO-IPS-Tomography). In Figure 1, the connection between NSO and IPS tomography is marked by dashed line to emphasize that photospheric magnetogram is not a necessary input. Comparisons are most sensible when the model combinations have some common parts. Limited by resources, not all acceptable magnetograms are run repeatedly for model upgrades.

In section 3, we specifically select a quiet period as the window of time for investigation and process the observation and simulation data for comparison. In section 4, we illustrate the variability of the model performance and compare them through visual inspection. Model validation is done for the time series of solar wind parameters (without and with normalization) and the statistics of solar wind parameters, magnetic field polarity, and slow-to-fast stream interactions in sections 5–8, respectively. Finally, we discuss and summarize our findings in section 9.

3. Data Process

We choose CRs 2056–2062 (about May–November 2007) as the time window considering three factors. First, full-rotation synoptic magnetograms from GONG, the only one accepted for all the above models, started to

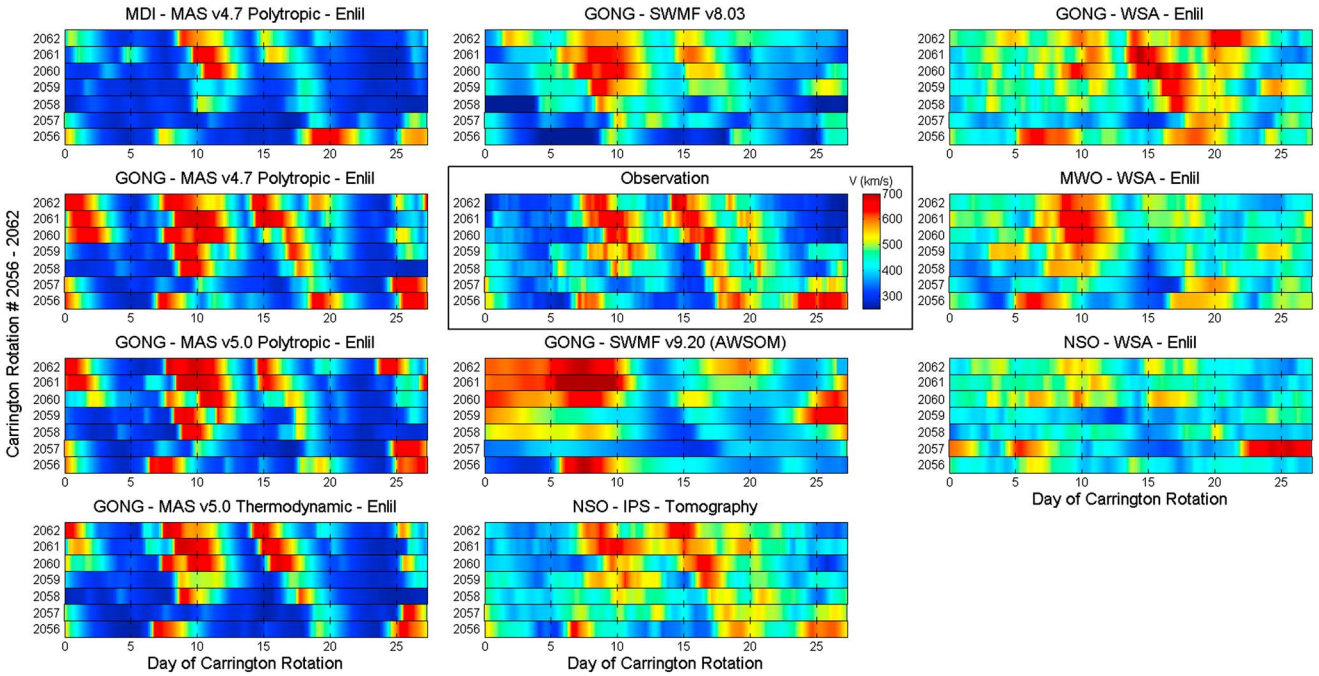

Figure 2. The comparison of 10 coupled models of the corona and heliosphere in reproducing solar wind speed *V* (color bar: 250–700 km/s) at Earth orbit. Each block is a stacked plot of seven CRs, with the abscissa for the day of each CR and the ordinate for CR 2056 to 2062. The block with a color bar and in the black box shows the hourly OMNI data from observation, smoothed using 5 h moving average. The other blocks are results from different models, with the name given at the top.

become available in late 2006. Second, year 2007 was in the late declining phase of a solar cycle but not yet in the deep solar minimum when the source surface is suggested to be lower than 2.5 R_υ normally used in the PFSS model [e.g., *Lee et al*., 2011] and when some of the fast wind is slower than 500 km/s [e.g., *Jian et al*., 2011b]. During CRs 2056–2062, only one CME hit Earth and it was on 21–22 May (http://www-ssc.igpp.ucla.edu/~jlan/ACE/Level3/ICME_List_from_Lan_Jian.pdf). This CME was slow with the highest speed of only 480 km/s. It occurred ahead of a fast wind and did not cause any big changes in solar wind parameters. Third, Ulysses had a fast latitudinal scan of ±60° (the range available from Enlil model) at 1.4–1.8 AU, and it was the last opportunity to observe the solar wind beyond the ecliptic plane. We will provide a validation for middle- to high-latitude solar wind using Ulysses and other spacecraft data in a follow-up study.

All the model runs are requested using the highest-resolution grids available at the CCMC's public Runs on Request system (http://ccmc.gsfc.nasa.gov/requests/requests.php). The grids vary much with models. For MAS coronal model, it is 101 × 101 × 128 (radial × latitude × longitude) in the polytropic version and 151 × 101 × 182 in the thermodynamic version for a region of 30 R_υ in radius, ±90° in latitude, and 360° in longitude. For WSA coronal model, the full-rotation synoptic magneograms have been smoothed to a longitudinal resolution of about 2.5°, i.e., 4 h. The Enlil model coupled with the WSA or MAS coronal model uses a uniform mesh of 1024 × 120 × 360 and 320 × 60 × 180 grid points, respectively, for a heliosphere of 2 AU in radius (with 21.5 or 30 R_υ subtracted), ±60° in latitude, and 360° in longitude. Converting the radial distance and radian degree to time using a solar wind speed of 400 km/s and a solar rotation of 27 days, the coarsest time resolution from the grids is about 5 h. The SWMF SC and IH components both use nonuniform grids with enhanced mesh refinement within 1.7 R_υ and at the sector boundary (for details see *Sokolov et al*. [2013] and *van der Holst et al*. [2014]), and their largest scale is shorter than 5 h. In addition, the time cadence from IPS tomography is 6 h. Therefore, we use hourly data from the Operating Mission as Nodes on the Internet (OMNI) [*King and Papitashvili*, 2005] and conduct a 5 h moving (boxcar) averaging centered at the current data point except intact for the first and last two data points of the whole data set. Meanwhile, we interpolate the simulation results into hourly data so that all the data have the same time cadence and can be put into a big matrix to facilitate comparison.

For each CR, to allow for solar wind propagation, we start the comparison with OMNI data 4 days later than the official start time used for synoptic maps and extend 4 days beyond the official end time. For CRs

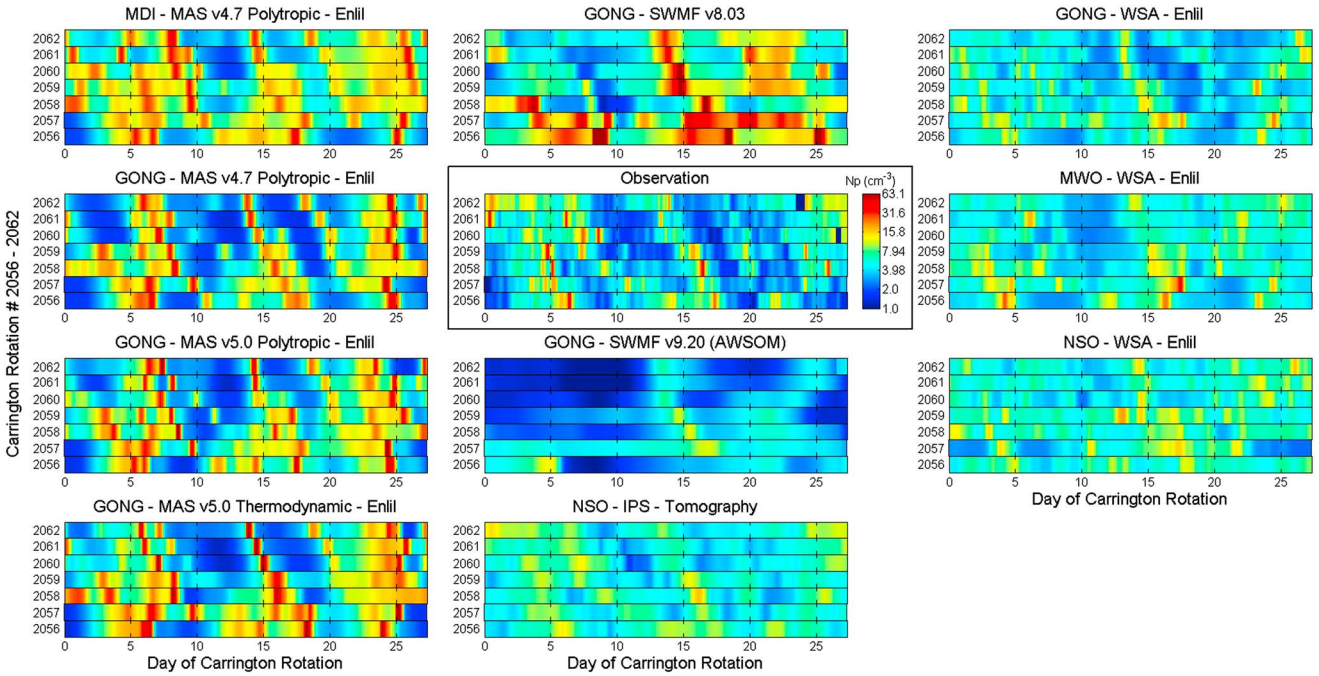

Figure 3. The comparison of 10 models in reproducing solar wind proton density N_p at Earth orbit. The caption of Figure 2 applies. The color bar indicates N_p of 1.0–63.1 cm^{-3} in a logarithmic scale.

2056–2062, the OMNI data from 1 May to 7 November in 2007 are used. Because models usually provide results starting right at the official start time of a CR and ending a few days beyond the end of a CR, we can make full use of the simulation results within each CR for comparison. However, the simulation data across CRs are choppy even after smoothing.

4. Visual Comparison

Solar wind speed V, proton number density N_p, magnetic field magnitude B, and proton temperature T_p are the fundamental solar wind parameters for space weather forecasting and for magnetosphere and ionosphere modeling; therefore, we choose to examine them. Figure 2 illustrates the large variability of the discrepancy of modeled solar wind speed from the observation. Each block is a stacked plot of seven CRs, with the abscissa for the day number in each CR and the ordinate for CR 2056 to 2062. The center block with a color bar and in the black box shows the OMNI data, and the other blocks plot the results from 10 model combinations with the model names given at the top. Blue is for slow wind, and red is for fast wind. Figures using monotonic color scheme is available to view online.

Among all the models, the GONG-MAS-Enlil model (regardless of version numbers) and NSO-IPS-Tomography seem to capture the time patterns of speed well, although the fast wind from the GONG-MAS-Enlil model and the slow wind from NSO-IPS-Tomography appear to be faster than observed. Many pairs of comparison can be conducted here. (1) Between the MAS v4.7 Polytropic-Enlil model using MDI versus GONG as input, the one using MDI as input misses several fast wind streams. (2) Using the same GONG input, the v4.7 and v5.0 of MAS polytropic-Enlil model both generate some false fast wind streams but at different times. (3) The difference between the GONG-MAS v5.0-Enlil model with polytropic implement or full thermodynamic energy equation is subtle and needs quantitative comparison to evaluate. (4) The GONG-SWMF model v8.03 matches with time patterns of speed roughly, while v9.20 misplaces the fast wind streams seriously and the fast wind from it lasts too long. (5) Among the WSA-Enlil model using GONG, MWO, NSO as input, the one using GONG captures the speed patterns best. The slow wind from all three runs is too fast. In addition, note the fast wind stream in CR 2059 is missing from NSO-WSA-Enlil probably due to a data gap of NSO for about 5 days. (6) Between the GONG-MAS-Enlil and GONG-WSA-Enlil models, the former appears to capture the time patterns and speed variation ranges better. Again, the GONG-MAS-Enlil model overestimates the fast wind speed, while the GONG-WSA-Enlil model overrates the slow wind speed.

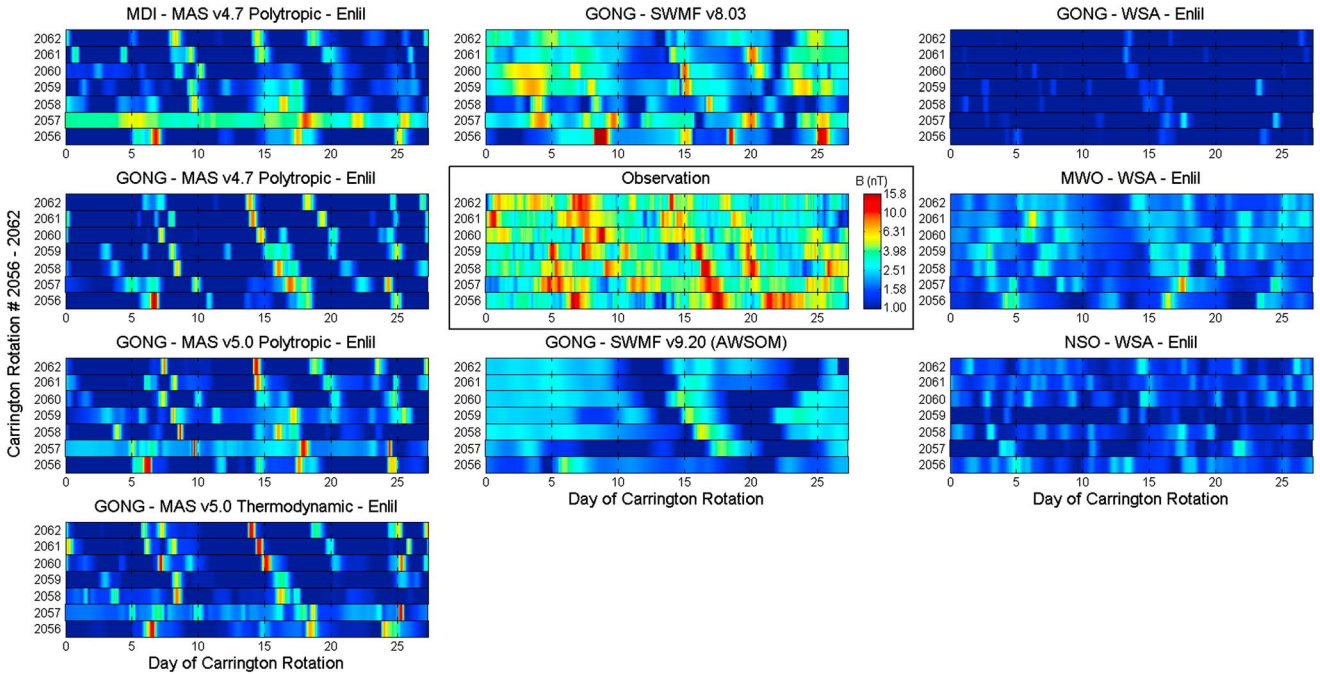

Figure 4. The comparison of nine models in reproducing the IMF magnitude *B* at Earth orbit. The caption of Figure 2 applies. The color bar indicates *B* of 1.0–15.8 nT in a logarithmic scale.

Similarly, the illustrative comparisons between OMNI (enclosed in the black box) and various models are provided in Figures 3–5 for N_p, B, and T_p, respectively. Due to the wide variation in range of these parameters, we use a logarithmic scale for the color bars in Figures 3–5. As expected, the performance of capturing the time patterns from each model is consistent with the one for V. From Figure 3, we can see the MAS-Enlil model (regardless of synoptic input and model versions) and GONG-SWMF v8.03 tend to

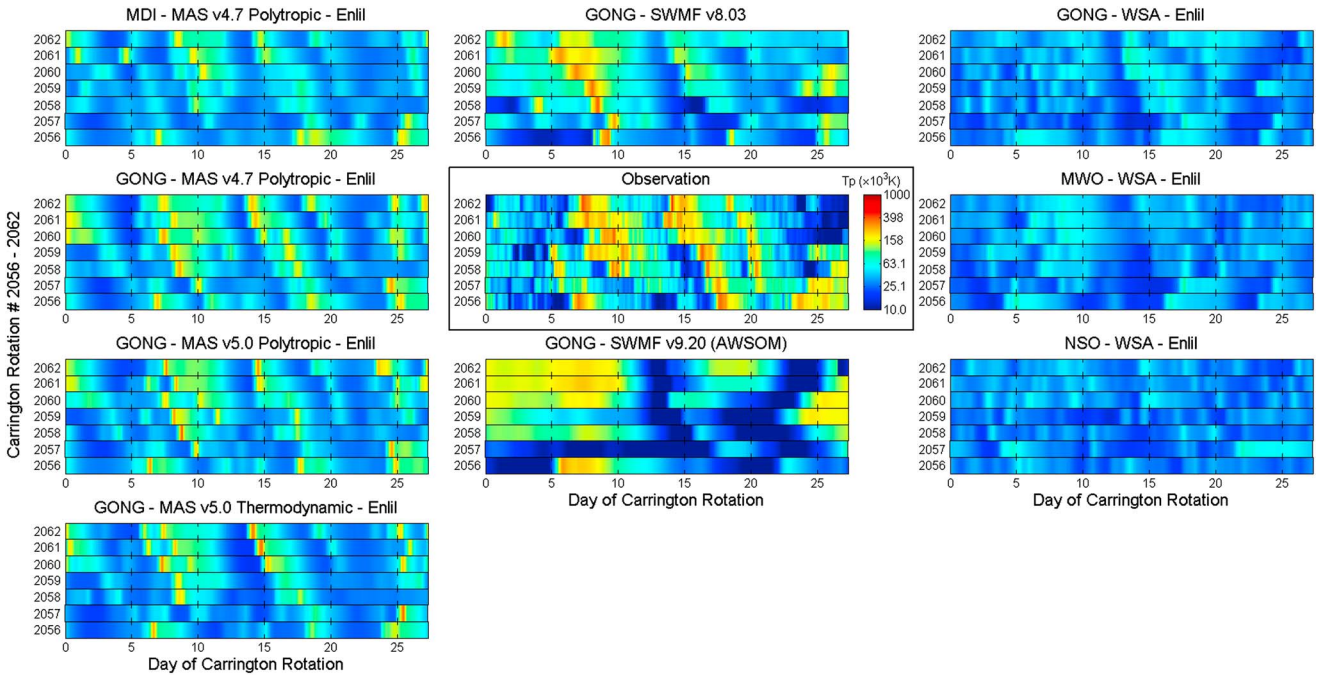

Figure 5. The comparison of nine models in reproducing the solar wind proton temperature T_p at Earth orbit. The caption of Figure 2 applies. The color bar indicates T_p of $10–1000 \times 10^3$ K in a logarithmic scale.

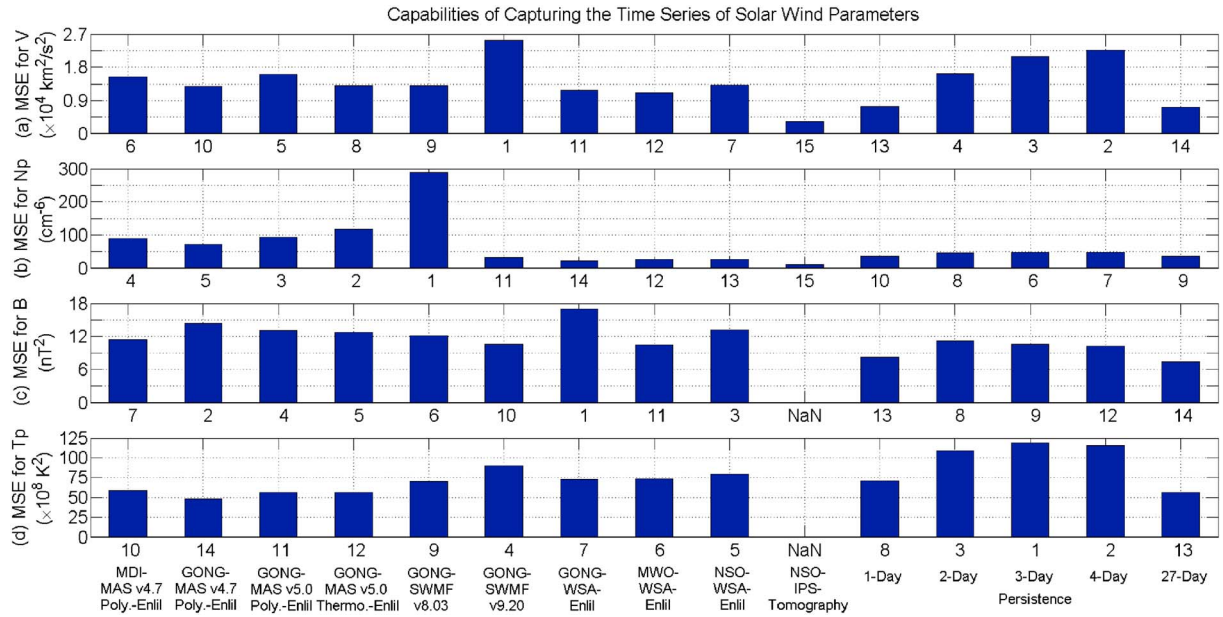

Figure 6. The comparison of 10 model combinations installed at the CCMC and 5 persistence models in capturing the time series of solar wind parameters during CRs 2056–2062. From top to bottom, the mean square errors (MSEs) between simulation and observation for (a) V, (b) N_p, (c) B, and (d) T_p. The ranking of the models is given at the bottom of each panel according to MSE. The lower the MSE, the higher the ranking.

overrate the N_p compression, while the WSA-Enlil model and IPS tomography seem to underrate the N_p compression and overestimate minimum N_p. NSO-IPS-Tomography does not currently provide B magnitude or T_p. All the remaining models seem to underestimate B for most of the time, especially the GONG-WSA-Enlil model, as shown in Figure 4. From Figure 5, we can see these models also appear to underestimate the maximum T_p, especially the WSA-Enlil model regardless of synoptic map input. The minimum T_p is often overrated by the models except GONG-SWMF v9.20.

The visual comparison above is informative and qualitative. In the following sections 5–8, we quantitatively validate the models from four aspects: the time series of solar wind parameters (without and with normalization), the statistics of these parameters, inward/outward magnetic field polarity and IMF SBs, as well as SIR arrivals and timing, although there are some common factors between these aspects.

5. Validation for Time Series of Solar Wind Parameters

A straightforward way to compare the time series of solar wind parameters between simulation and observation is to use the mean square error (MSE). For time series of parameter $x(t)$, $\mathrm{MSE} = \frac{1}{n}\sum_{t=1}^{n}[x_{\mathrm{modeled}}(t) - x_{\mathrm{observed}}(t)]^2$.

We rank the models according to MSE for each parameter, as shown in Figure 6. The lower MSE, the better the model captures time variations of that parameter, and the higher the ranking.

In addition, following *MacNeice* [2009b], we add persistence models as benchmarks in the comparison to characterize any benefit from using the more sophisticated models installed at the CCMC (hereafter called as "CCMC models" in short). For instance, the "1 day persistence" model assumes that the expected data are the same as the measured data 1 day before. We have considered six persistence models with 1 day, 2 day, 3 day, 4 day, 27 day, and 1-CR (27.2753 day) shifts, respectively. The results from 1-CR persistence model are nearly the same as the ones from 27 day persistence, so we do not show 1-CR persistence results additionally. For the vast space without continuous solar wind monitoring, it is necessary to use the CCMC models.

As shown in Figure 6, the results from CCMC models are generally better than 2–4 day persistence models for solar wind speed and temperature. The results from NSO-IPS-Tomography match with the observed time series of V and N_p best, better than any persistence model. The WSA-Enlil model runs (regardless of

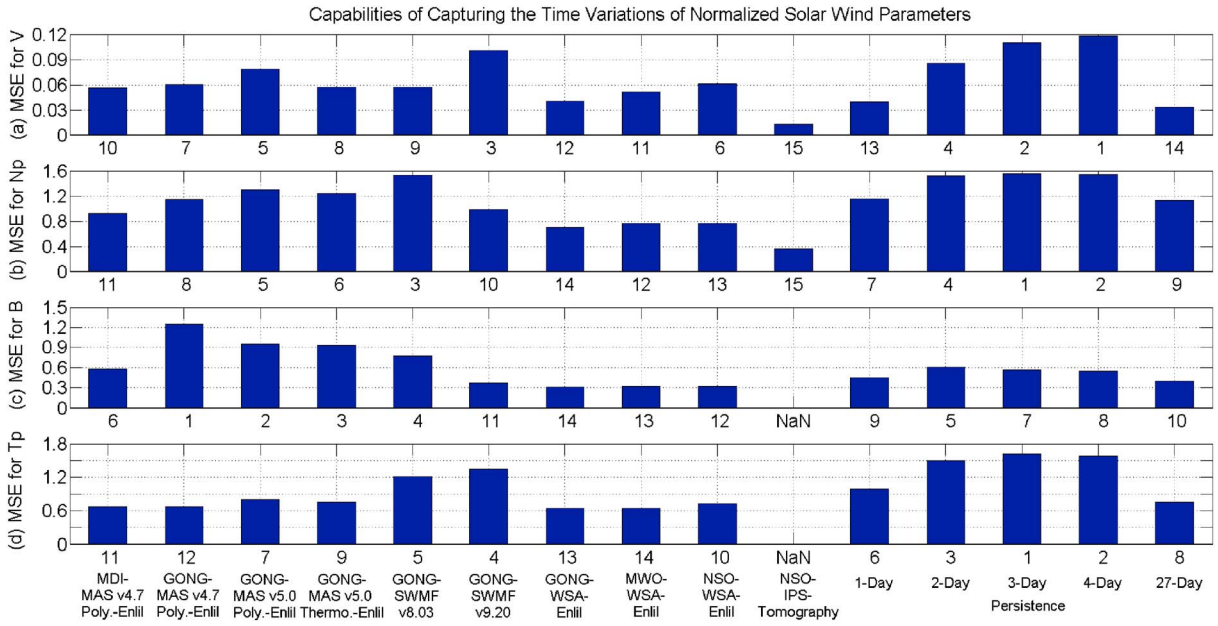

Figure 7. The comparison of 10 model combinations and 5 persistence models in capturing the time variations of normalized solar wind parameters during CRs 2056–2062. (a–d) The caption of Figure 6 applies. See section 5 for a detailed explanation of how Figure 7 complements Figure 6.

synoptic map input) match with time series of *V* and *B* well, while the MAS-Enlil model runs (regardless of synoptic map input or version numbers) match with the observed T_p well. For *V* and *B*, the 1 day and 27 day persistence models have lower MSEs than most other models.

There are two factors contributing to MSE: the discrepancy of parameter averages between models and observation and the discrepancy of time changes from the averages between models and observation. The first factor will be deliberated in the next section. To examine the second factor, for each data set and each parameter, we first obtain its average in each CR and then normalize the data by the average value in that CR. Next, we calculate the MSEs of the normalized data and rank the multiple models in Figure 7. There are significant changes from Figures 6 and 7. For example, the GONG-WSA-Enlil model has the largest MSE for *B* but the lowest MSE for normalized *B*, because the average *B* which largely disagrees with the observation (see Figure 12g) has been removed by normalization.

As displayed in Figure 7a, among the CCMC models, the NSO-IPS-Tomography has the lowest MSE off from the observation for the normalized *V*, while GONG-SWMF v9.20 has the largest MSE, related to its mismatch with time patterns of *V* illustrated in Figure 2. The CCMC models generally have lower MSEs than persistence models using the data taken 2–4 days before.

For normalized N_p, among the CCMC models, the GONG-SWMF v8.03 has the largest MSE, possibly related to its substantial overestimation of maximum N_p (see more in section 6). Among the other CCMC models, the NSO-IPS-Tomography and WSA-Enlil model (regardless of synoptic map input) have fairly low MSEs, indicating a good match with the time series of normalized N_p. The GONG-MAS-Enlil model runs, regardless of model versions, have large MSEs. Although the GONG-SWMF v8.03 matches with time patterns of N_p much better than v9.20 in Figure 3, it has much larger MSE for N_p and normalized N_p, demonstrating that we cannot solely depend on MSE to validate models. Similar to the performance for normalized *V*, the CCMC models generally match with normalized N_p better than 2–4 day persistence models. The IPS tomography and WSA-Enlil model match with normalized N_p even better than 1 and 27 day persistence models.

IPS tomography does not currently provide *B* magnitude or T_p. As illustrated in Figure 6c, among the remaining nine CCMC models, the WSA-Enlil model runs (regardless of synoptic map input) have similar and low MSEs for normalized *B*, better than all persistence models. The GONG-MAS-Enlil model runs (regardless of versions) tend to mismatch with time variations of normalized *B* more. As shown in Figure 7d, for normalized T_p, among the CCMC models, the WSA-Enlil model runs (regardless of synoptic

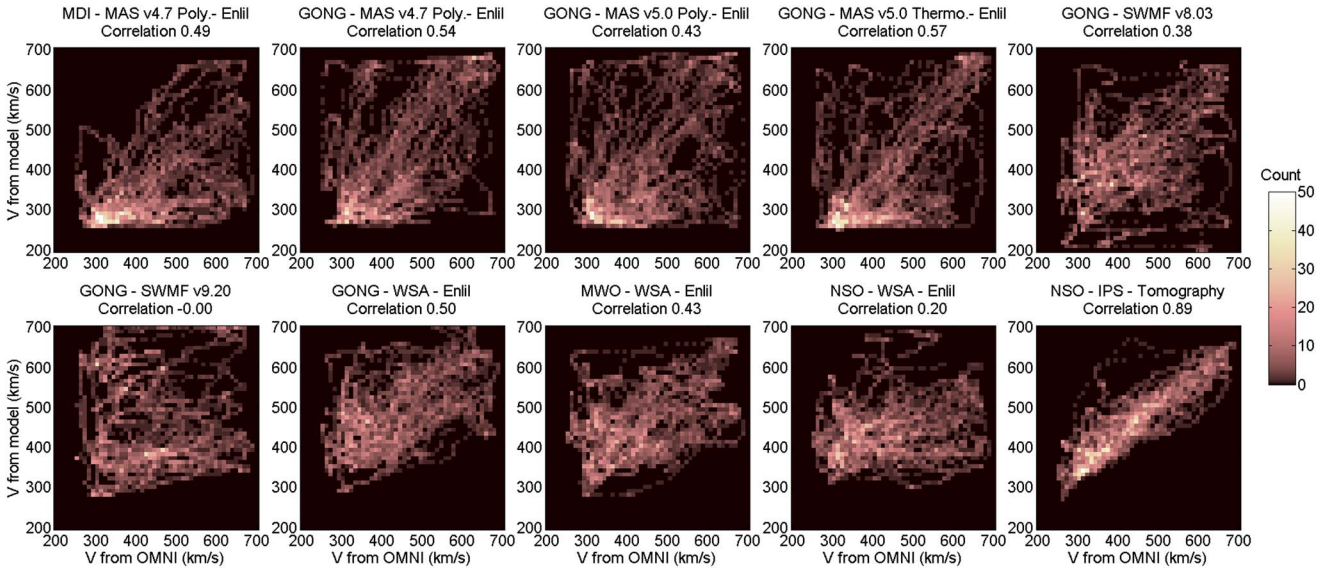

Figure 8. The distributions of occurrence with respect to the observed (abscissa) and modeled (ordinate) solar wind speed. The ranges in abscissa and ordinate are the same. Color indicates the counts from hourly data and ranges from 0 to 50. The bin size is 10 km/s. The cases with values higher than the last bin are counted in the last bin. The correlation coefficient between the observed and modeled solar wind speed is given at the top of each panel.

map input) and MAS-Enlil model runs (regardless of model versions) match with the observation well, while the two versions of GONG-SWMF model least. The CCMC models work better than the 2–4 day persistence models in matching with normalized T_p.

6. Validation for Statistics of Solar Wind Parameters

As mentioned above, the performance in reproducing the time series of solar wind parameters is related to how the models match with the average parameters. Hence, it is important to assess how well the models capture the statistics of solar wind parameters. Figures 8–11 illustrate the distributions of occurrence in the 2-D space defined by the observed and modeled values for V, N_p, B, and T_p, respectively. The ranges in abscissa and ordinate are the same, and the cases with values higher than the last bin are counted in the

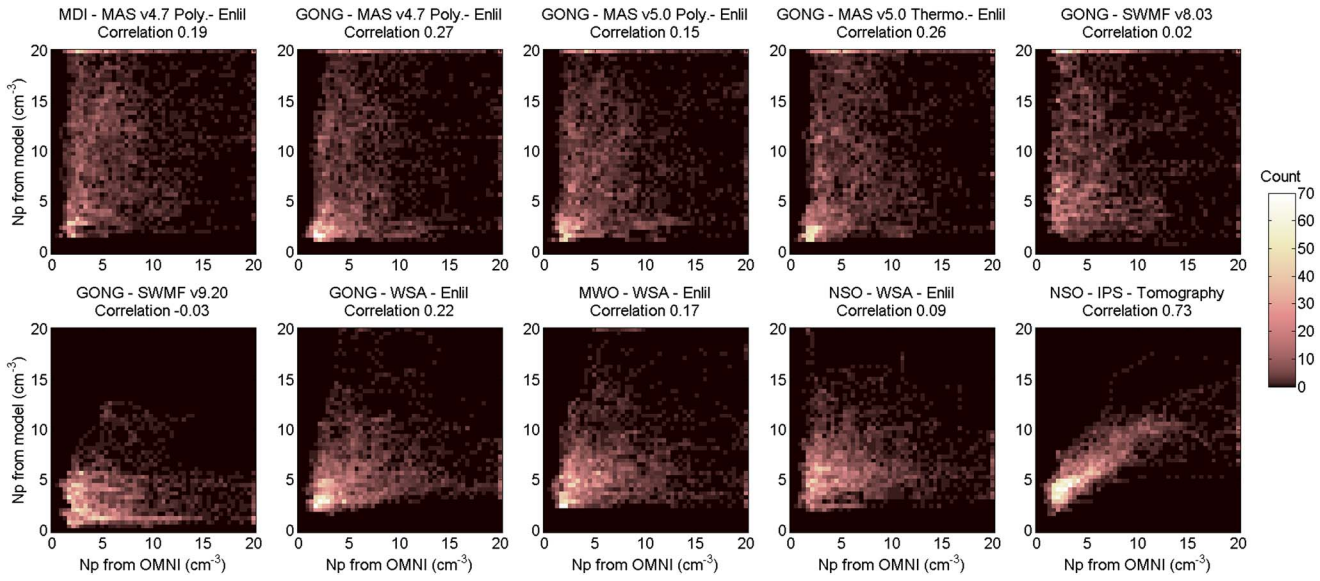

Figure 9. The caption of Figure 8 applies except this shows the solar wind proton number density. The bin size is 0.4 cm^{-3}. Color scale indicates the counts ranging from 0 to 70.

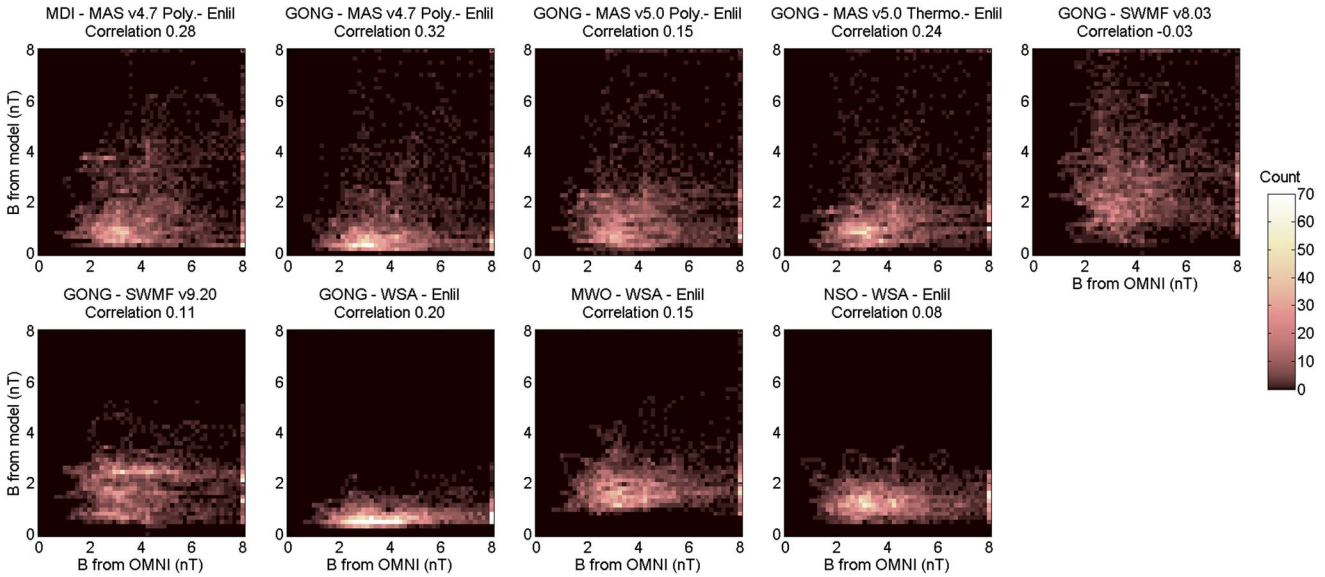

Figure 10. The caption of Figure 8 applies except this is for the IMF *B* magnitude. The bin size is 0.16 nT. Color scale indicates the counts ranging from 0 to 70.

last bin. The correlation coefficients between the observed and modeled parameters are listed as well. Because the persistence models use the same OMNI data set, they would match with solar wind statistics well. We do not consider them in this section.

The modeled *V* and N_p from the NSO-IPS-Tomography are better correlated with observations than the other models, with a correlation coefficient of 0.89 and 0.73, respectively. For *B* and T_p, the GONG-MAS v4.7 Polytropic-Enlil model has the highest correlation with observations among the models, with a correlation coefficient of 0.32 and 0.45, respectively, although it has larger MSEs for *B* and normalized *B* than many other models (Figures 6 and 7) and underestimates the median and minimum *B* largely (Figure 12). This again demonstrates it is important to validate models from multiple aspects. The same model correlates with observed N_p best too among the nine forward models using synoptic maps as input. Because the time patterns from the GONG-SWMF v9.20 model mismatch with observations most, it correlates with observations least for *V*, N_p, and T_p. Surprisingly, the GONG-SWMF v8.03 correlates with observed *B* least,

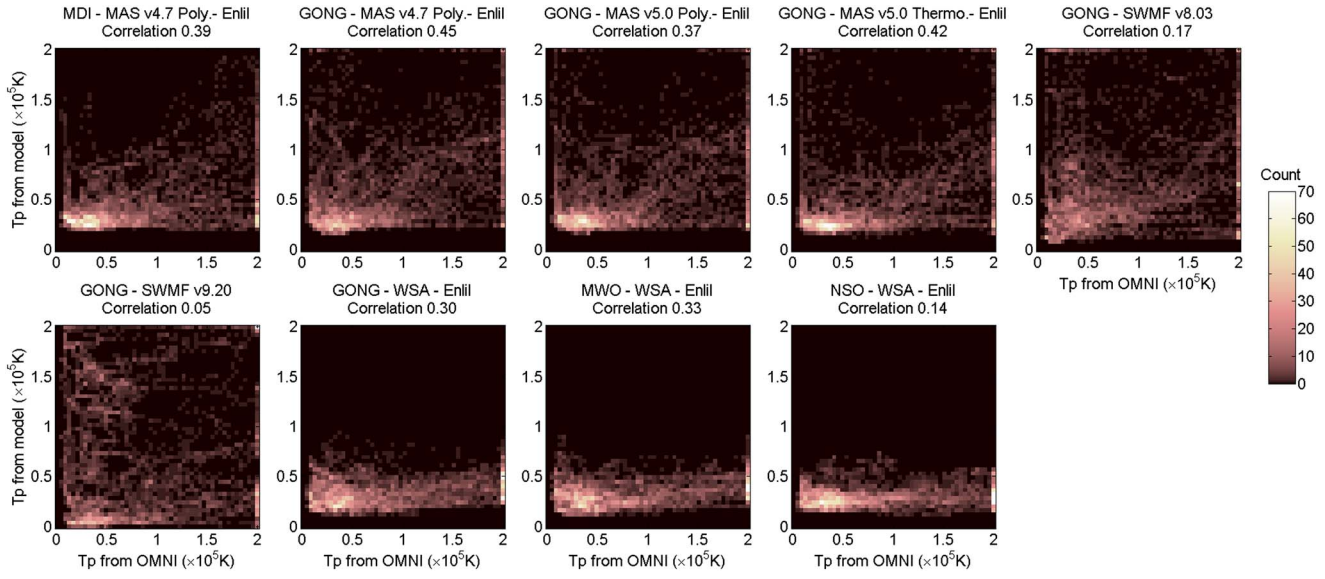

Figure 11. The caption of Figure 8 applies except this shows the solar wind proton temperature. The bin size is 4000 K. Color scale indicates the counts ranging from 0 to 70.

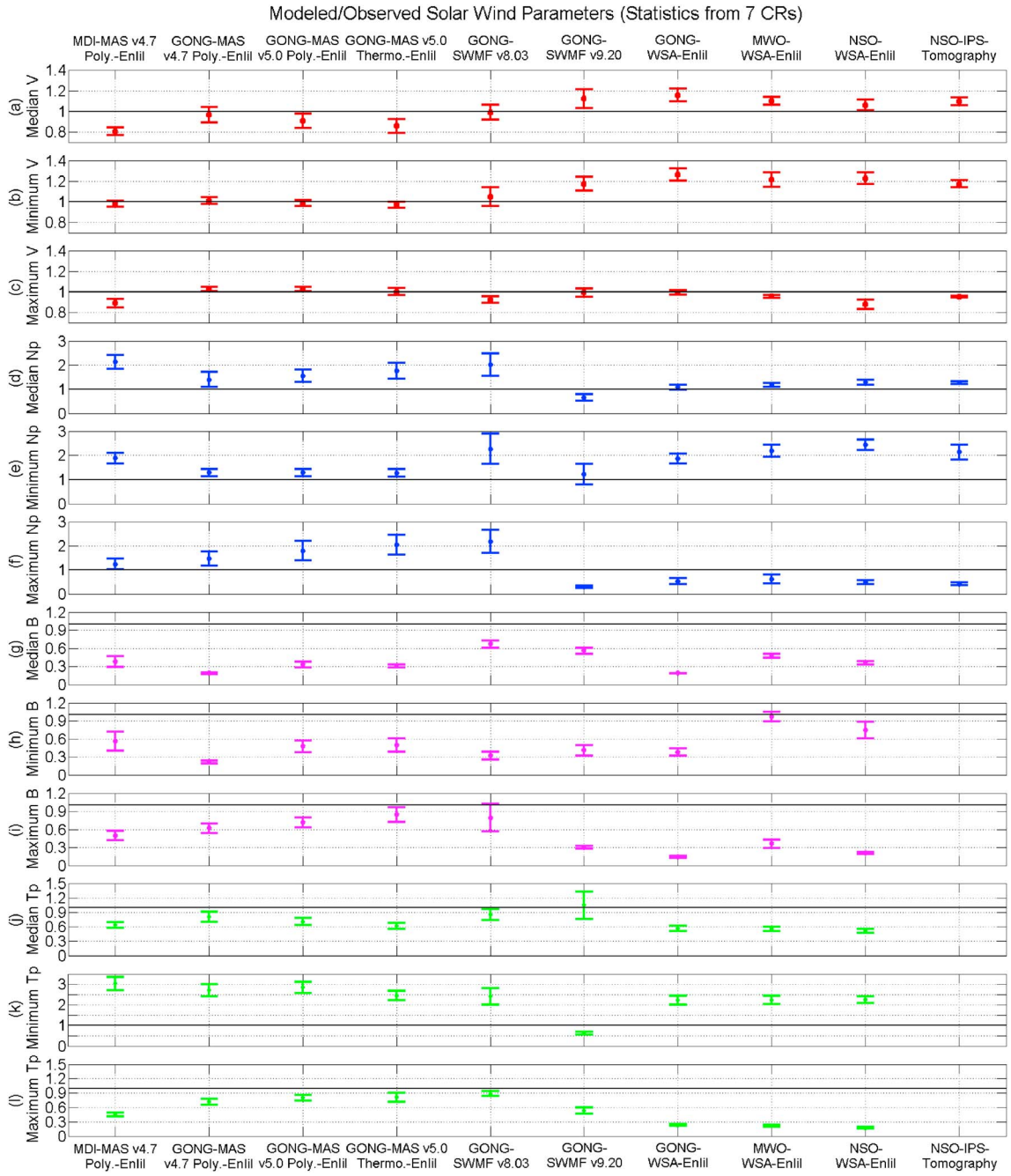

Figure 12. The ratios of median, minimum, and maximum solar wind parameters between model results and observations (modeled/observed). (a–c) Red for *V*, (d–f) blue for N_p, (g–i) magenta for *B*, and (j–l) green for T_p. The error bar is the standard error of the mean from seven CRs. The ordinate scales of median, minimum, and maximum are the same for the same parameter except for T_p. The solid black horizontal line in each panel marks the ratio of 1.

although it does not have largest MSE for *B* or normalized *B*. After implementing the full thermodynamic equations, the GONG-MAS v5.0-Enlil model correlates better with observations than the polytropic version for all the parameters.

Next we examine the median, minimum, and maximum values quantitatively. If we replace median with mean values, the comparison results are similar. For each parameter and each CR, we obtain the median, minimum, and maximum values from observation and simulation. Next, we calculate the ratios of modeled to observed values for each CR and then obtain the mean and standard error of the mean from the seven CRs. This method should be more robust than simply using the median, minimum, and maximum throughout the

seven CRs. Because V, N_p, B, and T_p often maximize in SIRs, we have also tried to compare the maxima of them for each SIR (identified in section 8). With more events for statistics, the results are analogues. Since the minima of these parameters are seldom in SIRs and SWMF v9.20's missing many SIRs would affect its performance, we use CR consistently to simplify the procedure.

Figure 12 shows the results from 10 model combinations: (a–c) red for V, (d–f) blue for N_p, (g–i) magenta for B, and (j–l) green for T_p. These models all match with the median, minimum, and maximum V within ±30%, better than with the other parameters. The MAS-Enlil model, regardless of solar input or versions, slightly underestimates the median V but matches with the minimum and maximum V well. The WSA-Enlil model, regardless of photospheric magnetogram sources, slightly overestimates the minimum and median V. The GONG-SWMF v8.03 model matches with the statistics of V well, while v9.20 overestimates the minimum and median V. The IPS tomography overestimates the minimum and median V but matches with the maximum V well. As the minimum and maximum V approximately present typical speed for slow and fast winds, the above assessment also indicates how well the models reproduce slow and fast winds.

As illustrated in Figures 12d–12f, the MAS-Enlil model overestimates the maximum and median N_p, regardless of solar input and versions. The WSA-Enlil model (regardless of magnetogram sources) and NSO-IPS-Tomography overestimate the minimum N_p and underestimate the maximum N_p, although match with the median N_p very well. These are consistent with Figure 3. After the upgrade from v8.03 to v9.20, the GONG-SWMF model changes from overestimating N_p to underestimating it except for its minimum.

As shown in Figures 12g–12i, all the models generally underestimate B, no matter its minimum, maximum, or median. In particular, the GONG-MAS v4.7 Polytropic-Enlil model underestimates the minimum B most, while the GONG-WSA-Enlil model underestimates the maximum B most. They both underestimate the median B most, by a factor of 5. The GONG-WSA-Enlil model in forecasting operational mode has been using a scaling factor of B to fix this issue, and a newer version of WSA-Enlil model would fix this too. The GONG-SWMF v8.03 model matches with the median B best, with about 30% underestimation, although it correlates with B least (Figure 10). Among the models, the GONG-SWMF v8.03 and GONG-MAS v5.0 Thermodynamic-Enlil models underestimate the maximum B least, while the MWO-WSA-Enlil model underestimates the minimum B least.

Models tend to overestimate the minimum T_p (approximately the slow wind temperature) except the GONG-SWMF v9.20 model, as displayed in Figures 12j–12l. All the models underestimate the maximum T_p (approximately the fast wind temperature), especially the WSA-Enlil model by 70% regardless of photospheric magnetogram sources, suggesting more coronal and/or solar wind heating needs to be implemented in the models for fast wind. The GONG-SWMF v8.03 model underrates the maximum T_p least, only by 10%. The GONG-MAS-Enlil model matches with the observed fast wind temperature second best, consistent with the results in *Riley et al*. [2011] which they attributed to the deliberate energy transport processes in their model. All the models underestimate the median T_p except the GONG-SWMF v9.20 model, which has much less temperature variation than observation and other models.

7. Validation for IMF Polarity

As demonstrated in Figure 4 of *MacNeice* [2009a], there are many short-term fluctuations of the magnetic field superimposed upon the long-term changes associated with the inward/outward sectors. Limited by the temporal and spatial resolutions, the models installed at the CCMC are built to reproduce only the large-scale magnetic configurations. To identify the main magnetic sectors, we filter the field polarity component from OMNI data and model output in the same way, using an algorithm revised on the basis of *MacNeice* [2009a] by trial and error.

This identification takes six steps to eliminate short excursions from the main sectors. (1) For OMNI data and NSO-IPS-Tomography, calculate the Parker spiral angle ϕ with respect to the radial direction, where 0° is along the radial outward direction. For Earth, the radial and tangential magnetic field components can be approximated by $-B_x$ and $-B_y$ in the geocentric solar ecliptic coordinate, where X axis points from the Earth toward the Sun, Y axis points toward dusk in the ecliptic plane, and Z axis is parallel to the ecliptic pole. If $-135° \le \phi \le 45°$, the magnetic field polarity is set to be -1 (outward), otherwise 1 (inward). For other models, magnetic field polarity is an output parameter and has the same outward or inward meaning as

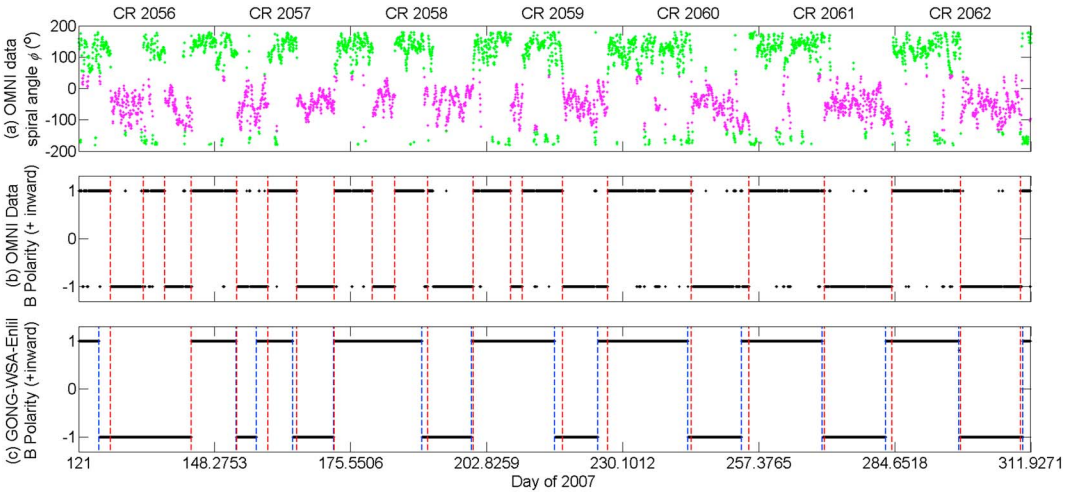

Figure 13. Time variations of (a) the IMF Parker spiral angle ϕ in the ecliptic plane; the magnetic field polarity from (b) OMNI data and (c) GONG-WSA-Enlil model during CRs 2056–2062. In Figure 13a, magenta and green dots are for $-135° \le \phi \le 45°$ and outside the range, respectively. In Figures 13b and 13c, 1 for inward polarity while -1 for outward polarity. In Figure 13b, the red dashed lines mark the SBs from observation. In Figure 13c, the blue dashed lines indicate SBs from the model, and the red dashed lines mark the matching SBs from observation.

defined above. (2) For any single data point which has at least a 3 h period of opposite polarity on each side, set its polarity the same as the surrounding. (3) Group each contiguous block of same magnetic field polarity as one magnetic field sector. (4) For any period of field reversal which is not longer than $\tau = 2$ h and is separated from the closest reversal by at least 3τ on either side, set its polarity the same as the neighboring polarity and regroup the magnetic field sectors. (5) Repeat Step (4) in turn for $\tau = 4, 6, \ldots, 12$ h. (6) For any sector lasting no longer than 24 h, set its polarity the same as the neighboring polarity. Although the above six-step filtering does not affect the model output much, it removes a few short excursions of the magnetic field and keeps the main sectors for comparison. Figure 13 shows the Parker spiral angle from OMNI data, the magnetic field sectors and SBs from OMNI data and GONG-WSA-Enlil model, as an example. For each model, we find the closest SB from observation with the same direction of polarity reversal for each modeled SB.

Figure 14 illustrates the comparison of IMF sectors from the OMNI data and 10 model combinations installed at the CCMC, in a format similar to Figure 2. Using OMNI data, two fewer polarity reversals were observed in CRs 2060–2062 than in the previous four CRs, presenting the transition from four-sector to two-sector structure, related to the flattening out of the sector boundary with the declining of solar activity cycle. The GONG-MAS v5.0 Polytropic-Enlil model captures the exactly right amount of sectors for each CR. Although the GONG-SWMF v9.20 misplaces the locations of fast and slow winds seriously in Figures 2–5, its match with the IMF sectors is correctable. The NSO-WSA-Enlil model misses the sector changes in CR 2059, possibly attributed to the NSO data gap aforementioned. However, this data gap does not affect the result from NSO-IPS-Tomography, probably because the data gap is interpolated across in UCSD's spline fit (see section 2). In addition, the sector durations from the NSO-IPS-Tomography seem to disagree with OMNI data largely in CRs 2058–2059 and 2061–2062, while the durations from the NSO-WSA-Enlil model disagree with OMNI data largely in CRs 2056–2057. The difference is possibly because NSO-IPS-Tomography uses the daily updated magnetograms and CSSS model, while NSO-WSA-Enlil uses the CR synoptic maps and PFSS model. The main difference between the CSSS and PFSS models is that the former includes the effects of horizontal and sheet currents existing in the real corona [e.g., *Poduval and Zhao*, 2014, and references therein]. From the comparison, we can only conclude there is no superior one between the two models and the performance depends on CR.

As introduced in section 5, we add five persistence models with 1–4 and 27 days shift as benchmarks in the comparison, applying the same six-step algorithm to identify their IMF sectors. For each model, we calculate the time fraction of matching IMF polarity between model results and observations. As shown in Figure 15a, this time fraction ranges from 70% to about 90% for CCMC models, higher than the 3 and 4 day persistence

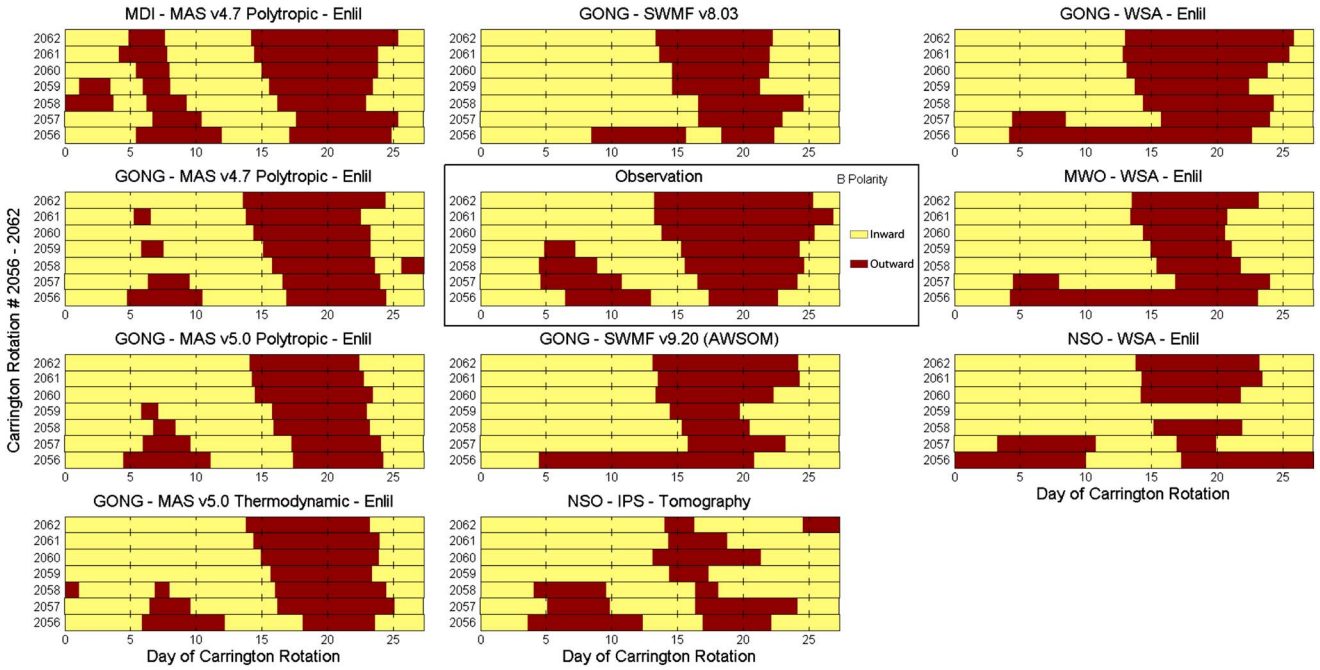

Figure 14. The comparison of 10 model combinations in reproducing the IMF polarity at Earth orbit, brown for outward and yellow for inward. The caption of Figure 2 applies.

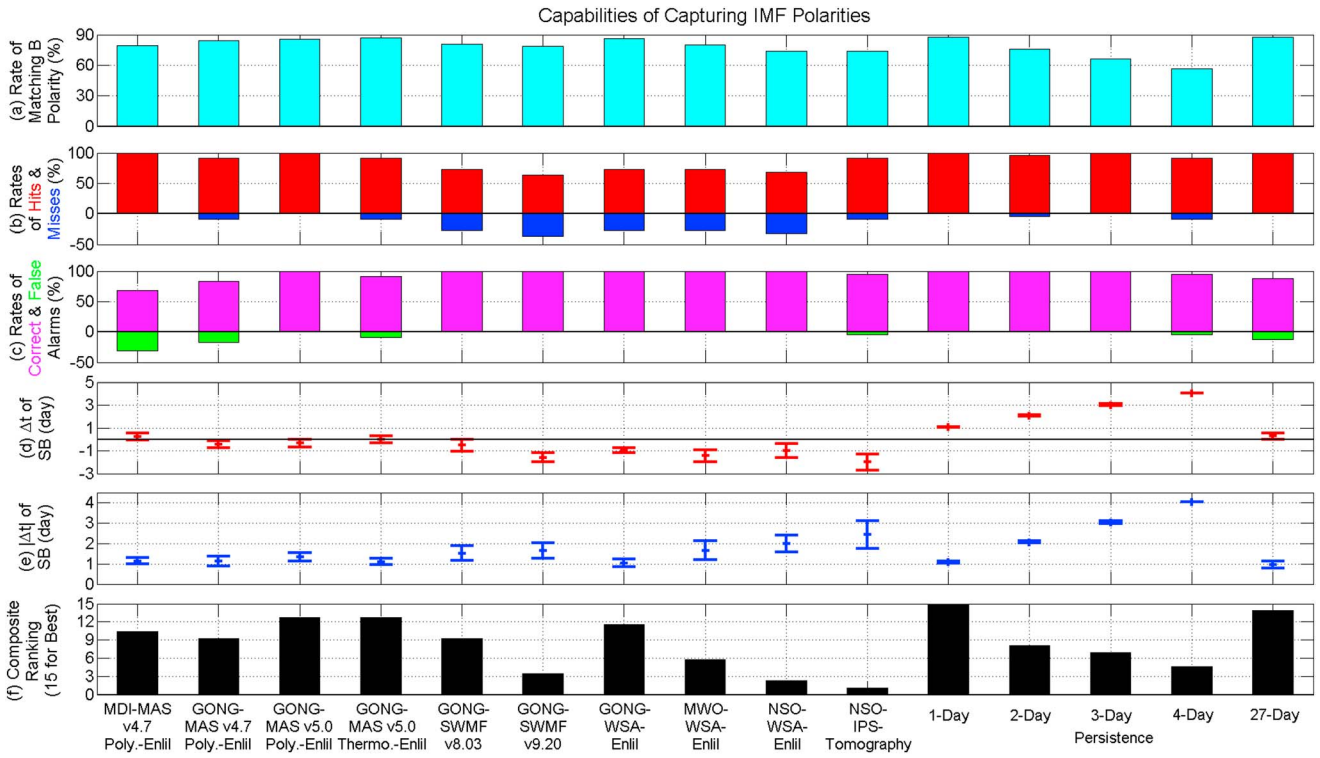

Figure 15. The comparison of 10 model combinations and 5 persistence models in reproducing the IMF polarities and matching SB timing. (a) The time fraction of matching IMF polarity with the observation, (b) the rates of hits (red, >0) and misses (blue, <0) among the observed SBs, (c) the rates of correct (magenta, >0) and false (green, <0) positive alarms among modeled SBs from each model combination, (d) the mean (red cross) and standard error of the mean (red error bar) for time discrepancy (modeled-observed) of SBs, the solid black horizontal line for 0, (e) the mean (blue cross) and standard error of the mean (blue error bar) for absolute time discrepancy of SBs, and (f) the composite ranking based on Figures 15a–15e where a weight of ½ is used for the standard error of the mean.

models. Among the CCMC models, the NSO-WSA-Enlil and NSO-IPS-Tomography match with the observed polarity least, by 74%. Next, we calculate the rates of hits and misses among the observed SBs, and the rates of correct and false alarms among the modeled SBs. The MDI-MAS v4.7 Polytropic-Enlil and GONG-MAS v5.0 Polytropic-Enlil models capture all the SBs, while the GONG-SWMF v9.20 misses SBs most often as high as 36%. Nearly all the modeled SB alarms are true positives for the CCMC models except the MAS v4.7 Polytropic-Enlil model using MDI and GONG as input, which has false positive alarm rates of 31% and 17%.

By comparing the SB timing, we obtain the time discrepancy $\Delta t = t_{\text{modeled}} - t_{\text{observed}}$ between modeled and observed SBs, and the absolute time discrepancy $|\Delta t|$. Negative Δt indicates earlier arrival than observed, which is what most CCMC models predict, with the exception of the MDI-MAS v4.7 Polytropic-Enlil and GONG-MAS v5.0 Thermodynamic-Enlil models which have nearly equal likelihoods predicting earlier and later arrivals. The GONG-WSA-Enlil model has the smallest $|\Delta t|$ of 1 day. Among the CCMC models, the NSO-IPS-Tomography results have the largest time discrepancies from observations with largest error bars (the standard error of the mean), possibly caused by the use of daily updated NSO magnetogram, CSSS model, and spline fit interpolation. The 1 to 4 day persistence models produce SB late by 1–4 days correspondingly. The 27 day persistence model has small time discrepancy, but it has a false positive alarm rate of 12%. Combining the rankings of the above five factors (rate of matching polarity, rate of hits, rate of correct positive alarms, absolute magnitude of Δt, and $|\Delta t|$) with the same weight and the error bars of Δt and $|\Delta t|$ with half of the weight, we obtain the composite rankings of the 10 models in Figure 15f. The 1 and 27 day persistence models are ranked high, benefited from the quasi-steady solar wind and IMF sector structures in the declining phase of solar cycle 23. Among the CCMC models, the GONG-MAS v5.0 (polytropic and thermodynamic)-Enlil and GONG-WSA-Enlil models capture the IMF polarity and the polarity changes well, while the NSO-IPS-Tomography, NSO-WSA-Enlil, and GONG-SWMF v9.20 models not so well.

Although the above models are currently not constructed to capture the magnetic field out of ecliptic plane, we have examined the model performance for capturing the B_z direction to gain some general knowledge. Whether using hourly or daily averaged data, the success rates are about 50% for all the models, similar to random prediction, as expected. *Zhang and Moldwin* [2014] found about 37% of long-period (>6 h) southward B_z (<-10 nT) intervals were in the background solar wind and not associated with CMEs or small-scale flux ropes. Further studies of the formation of such phenomena are needed to make progress on predicting B_z in quiet solar wind. In addition, with respect to the model resolution of a few hours, the long-period southward B_z intervals are short. Higher-resolution photospheric magnetogram input and models are required to resolve them.

8. Validation for Slow-to-Fast Stream Interactions

Because solar wind speed is a robust parameter every model can provide and it has the best observational coverage, we use it to identify the SIRs. The algorithm for automatic detection is revised based on *Owens et al*. [2005] and *MacNeice* [2009a], and it includes 10 steps. We have applied the algorithm to observations and each model result to assure major SIRs are successfully captured. (1) Mark all time points which are more than 50 km/s faster than 1 day earlier. (2) Eliminate any isolated single data points which are marked. (3) Group each contiguous block of marked points as a distinct high speed enhancement (HSE) and find the start and end time of each HSE. (4) For each HSE, find the minimum speed starting 2 days ahead of the HSE till the start of the HSE, and mark it as the minimum speed (V_{min}) of the HSE; find the maximum speed starting from the beginning of the HSE through 1 day after the HSE and mark it as the maximum speed (V_{max}) of the HSE. (5) For each HSE, find the last time reaching V_{min} and the first time reaching V_{max} and mark them as the start and end time of an SIR. (6) Combine SIRs separated by less than 0.75 day and eliminate any repeated count of SIRs. (7) Reject any SIRs shorter than 0.5 day. (8) For the regrouped SIRs, find the V_{min} and V_{max} for each SIR and mark the last time of highest speed gradient as the stream interface (SI), the boundary between slow and fast wind. Eliminate SIRs with the redundant SI time. (9) Reject any SIRs with V_{min} faster than 500 km/s, or V_{max} slower than 400 km, or speed increase less than 100 km/s. (10) Reject SIRs crossing two CRs because the simulation results are choppy crossing two CRs even after smoothing.

Figure 16 shows the SIRs detected using the algorithm for OMNI data and the GONG-WSA-Enlil model, as an example. For each simulated SIR, we find the closest SI from observation. If there is no matching SI,

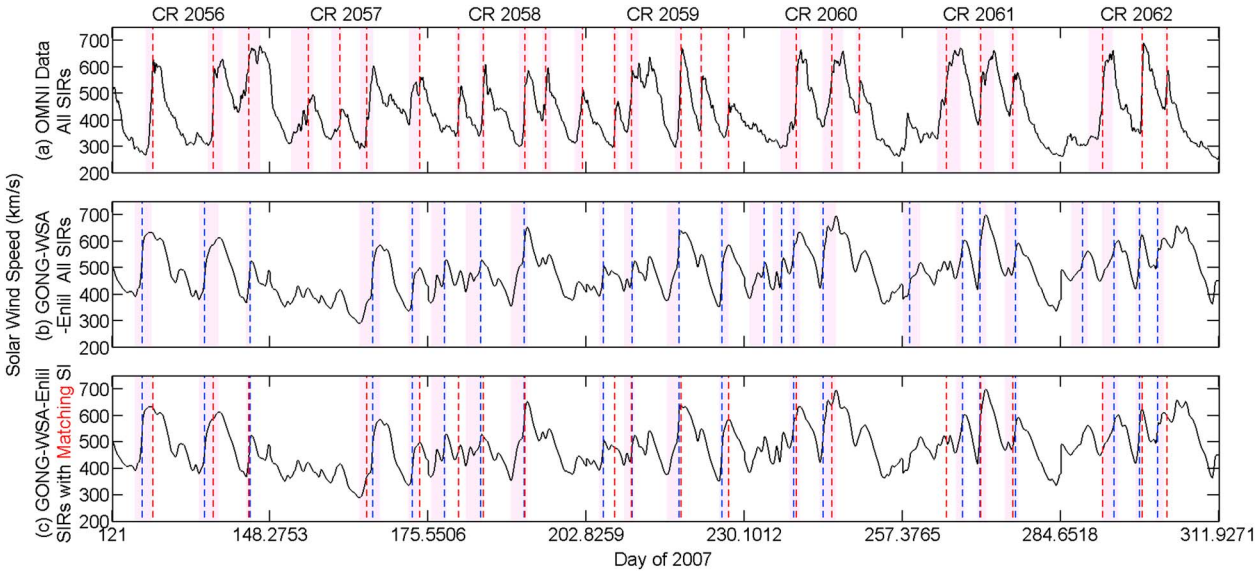

Figure 16. Time variations of solar wind speed during CRs 2056–2062 from (a) OMNI data and (b, c) GONG-WSA-Enlil model. Regions shaded in magenta indicate SIRs. In Figure 16a, the red dashed lines mark the SIs from observation. In Figures 16b and 16c, the blue dashed lines indicate SIs from the model, and the red dashed lines mark the matching SIs from observation. In Figure 16c, only SIRs with matching SIs are shaded in magenta.

the simulated SIR is removed from further comparison. For each model, we calculate the rates of hits and misses among all observed SIRs, the rates of correct and false alarms among all simulated SIRs, as displayed in Figures 17a and 17b. Same as above, we add five persistence models with 1–4 and 27 day shift for comparison. The prediction of SIR arrivals is more complicated than IMF polarities, and the success rate is lower as expected. Among the CCMC models, the GONG-MAS v4.7 Polytropic-Enlil model, GONG-WSA-Enlil model, and NSO-IPS-Tomography have the equally highest rates of hits, which are about 77%, while the GONG-SWMF v9.20 and NSO-WSA-Enlil model have high rates of misses, 69% and 50%, respectively. The 1 and 27 day persistence models capture SIRs more than 80% of time, as expected because the solar wind is quasi-steady in the late declining phase. All the simulated SIRs from the GONG-SWMF model (both versions) and IPS tomography are correct positive alarms. For GONG-SWMF v9.20, it is because not many SIRs are predicted by this new version. The GONG-MAS (v4.7 and v5.0) Polytropic-Enlil and GONG-WSA-Enlil models have high false positive alarm rates of about 17%, comparable to the false-alarm rates of 2 and 4 day persistence model and lower than the 3 day persistence model.

By comparing the SI timing from observation and simulation, we obtain the time discrepancy $\Delta t = t_{\text{modeled}} - t_{\text{observed}}$ between models and observation and the absolute time discrepancy $|\Delta t|$. The mean and standard error of the mean from two dozens of SIRs for each model are plotted in Figures 17c and 17d. On average, the MAS-Enlil model tends to predict later arrival than observed, regardless of versions or synoptic map input, possibly related to its underestimation of median V (Figure 12). The GONG-WSA-Enlil model and NSO-IPS-Tomography tend to predicate slightly earlier arrivals. Both the GONG-SWMF v8.03 and MWO/NSO-WSA-Enlil models have nearly equal chances predicting earlier and later arrivals. In contrast, the 1, 2, and 27 day persistence models predict later arrivals while 3 and 4 day persistence models predict earlier arrivals. In terms of $|\Delta t|$, the NSO-IPS-Tomography captures the SI timing best within an error of about half a day. The GONG-SWMF v9.20 and NSO-WSA-Enlil models have the largest time offset, by more than 2 days, with large error bars. The great difference in the performance of NSO-WSA-Enlil model for Δt and $|\Delta t|$ suggests both Δt and $|\Delta t|$ are needed in model validation. The time predictions from other models are off by about 1 day, more than the time prediction discrepancies for some CMEs [e.g., *Colaninno et al.*, 2013; *Millward et al.*, 2013; *Vršnak et al.*, 2014; *Mays et al.*, 2015]. The $|\Delta t|$ for persistence models ranges from 1 to 2 days, related to the time shift used in the models.

In Figure 17e, the 10 CCMC model combinations and 5 persistence models are ranked, considering the above four factors (rate of hits, rate of correct positive alarms, absolute magnitude of Δt, and $|\Delta t|$) and using a half weight for the standard error of the mean for Δt and $|\Delta t|$. Overall, among the CCMC models,

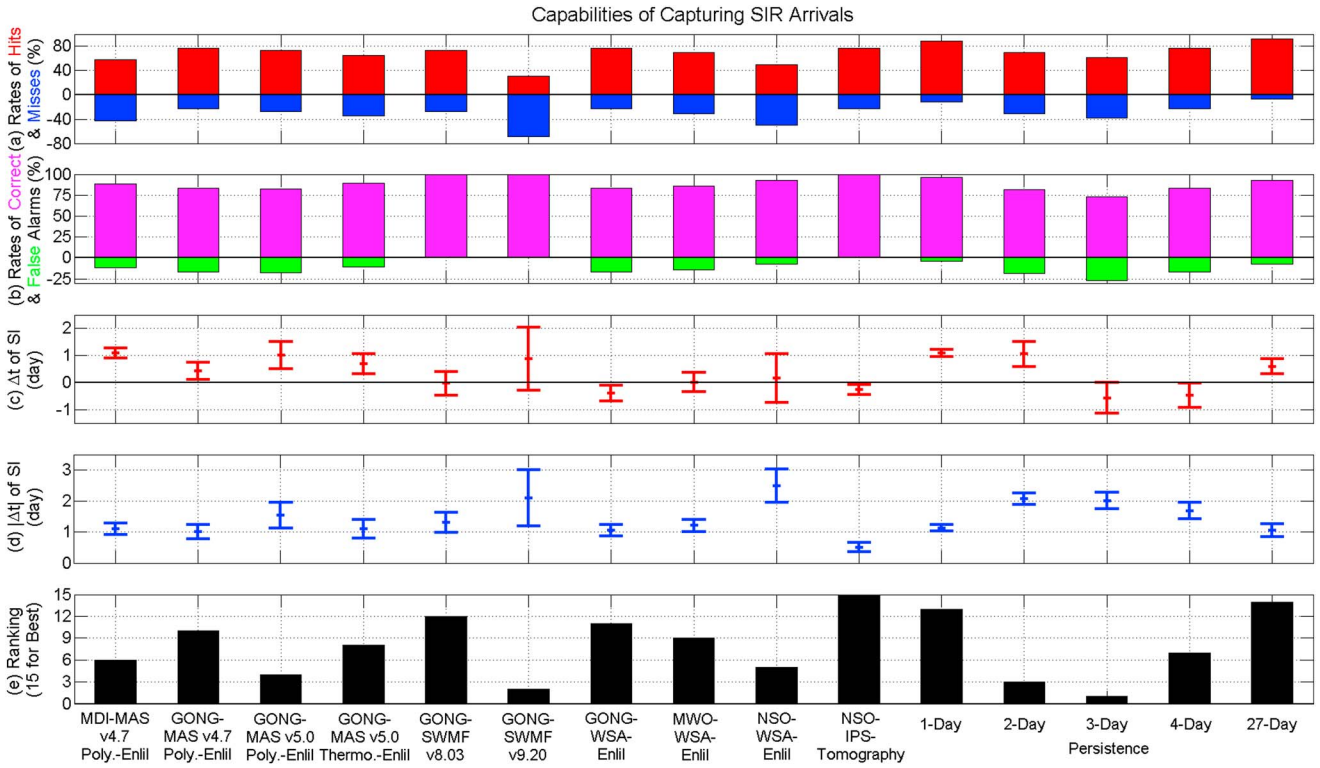

Figure 17. The comparison of 10 model combinations and 5 persistence models in capturing SIRs and matching SI timing. From top to bottom, (a) the rates of hits (red, >0) and misses (blue, <0) among the observed SIRs, (b) the rates of correct (magenta, >0) and false positive alarms (green, <0) among modeled SIRs from each model combination, (c) the mean (red cross) and standard error of the mean (red error bar) for time discrepancy (modeled-observed) of SIs, (d) the mean (blue cross) and standard error of the mean (blue error bar) for absolute time discrepancy of SIs, and (e) the composite ranking based on Figures 17a–17d where a weight of ½ is used for the standard error of the mean.

the NSO-IPS-Tomography, GONG-SWMF v8.03 and GONG-WSA-Enlil models capture SIRs and match with SI timing best, while the GONG-SWMF v9.20 and GONG-MAS v5.0 Polytropic-Enlil models disagree with observations most. Although the 1 day persistence model captures SIRs well with high rankings, it has large Δt and short warning time. The 27 day persistence model performs well, heavily depending on the quasi-steady solar wind patterns. We will evaluate this for a more active solar cycle phase in the future. All the models except the GONG-SWMF v9.20 model reproduce the duration of SIRs well (not illustrated), within ±0.5 day, suggesting good capturing of rising slopes for solar wind speed.

9. Conclusions and Discussion

We have developed performance metrics for solar wind simulation and applied them to 10 model combinations for the late declining phase of solar cycle 23. There are some common factors among the aspects addressed in sections 5–8. To summarize the validation results, in Table 1, we compile the general strengths and weaknesses of each model installed at the CCMC. Because persistence models are not the focus of this study, they are excluded in the comparison. This diagnosis can be an unbiased reference for model developers and users.

The current capturing of B_z direction from all the models is like random prediction, because the models are not constructed to get B_z and B_z in the solar wind varies frequently. For IMF magnitude, all the models underestimate it, no matter its minimum, maximum, or median, especially the GONG-WSA-Enlil model, which has been using a scaling factor to magnify B in the operational mode. A new version of WSA-Enlil model at the CCMC will include this scaling factor too. All the models underestimate the fast wind temperature while generally overestimate the slow wind temperature. The WSA-Enlil model (regardless of magnetogram sources) underrates the fast wind temperature by 70% and requires significant heating to be added. The inclusion of various energy transport processes in MAS v5.0 coronal model [e.g., *Riley et al.*, 2011]

Table 1. Summary of Model Evaluation

Synoptic Map	Model: SC Part	Model: IH Part	Strength		Weakness	
MDI	MAS v4.7 Polytropic	Enlil	Matching with SB timing well		Missing fast wind streams in three CRs, highest false-alarm rate for SBs	Overestimating maximum and median N_p; overestimating minimum T_p most
GONG	MAS v4.7 Polytropic	Enlil	Correlating with B and T_p best, matching with statistics of V well, and matching with time series of T_p best		Mismatching with time series of normalized B most; underestimating minimum B most	
GONG	MAS v5.0 Polytropic	Enlil	Capturing the occurrence of SBs best with no flase alarm	Capturing the time patterns of solar wind parameters well, capturing IMF polarities and SBs best	Highest rate of false alarms for SIRs	
GONG	MAS v5.0 Thermo-dynamic	Enlil	Matching with maximum B and SB timing best			
GONG	SWMF v8.03		Matching with median V and B and maximum T_p best; SIRs second best		Matching with time series of N_p least, overestimating maximum N_p most, largest uncertainty for N_p estimation, correlating with B least, and missing SBs in three CRs	
GONG	SWMF v9.20		Matching with median T_p best		Capturing time patterns of solar wind parameters least, correlating with V, N_p, and T_p least, underestimating maximum N_p most, missing SBs and SIRs most, largest uncertainty for SI timing prediction	
MWO	WSA	Enlil	Matching with median N_p best	Capturing the time series of normalized solar wind parameters well	Underestimating maximum B most by 80%	Overestimating slow wind V and T_p, underestimating maximum N_p and B, underestimating maximum T_p by ~70% and median T_p by ~40%
MWO	WSA	Enlil	Underestimating minimum B least			
NSO	WSA	Enlil			Missing time patterns of solar wind parameters, missing SIRs in two CRs, overestimating minimum N_p most, and largest absolute time discrepancy for SIs	
NSO	IPS Tomography		Capturing time patterns of V well, matching with time series of V and N_p best, correlating with V and N_p best, and capturing SIRs and SI timing best		Overestimating slow wind V, matching with IMF polarity and SB timing least, large discrepancy for the durations of IMF sectors	

and SWMF v8.03 model [*van der Holst et al*., 2010] have resulted in their better match with fast wind temperature than other models.

Among the 10 model combinations installed at the CCMC, the NSO-IPS-Tomography correlates with solar wind V and N_p best, reproduces the time series of V and N_p best, and captures the SIRs and SI timing best. However, it uses the remote sensing measurements of solar wind fluctuations therefore at a different starting point from other forward models starting from photospheric maps. For space weather operation, the IPS tomography would have a shorter warning time by the difference (about 1 day) between the solar surface and the inner location of IPS source observed closest to the Sun at about 40 R_υ (e.g., *Jackson et al*. [2015] for details). In the models using the same synoptic photospheric magnetograms from GONG, the MAS v5.0 (polytropic and thermodynamic)-Enlil model captures time patterns of solar wind parameters and SBs best; the SWMF v8.03 matches with median V, median B, and maximum T_p best; the WSA-Enlil model matches with median N_p, time series of normalized N_p and B best. The MAS-Enlil model, regardless of synoptic map input or coronal model version, tends to overestimate maximum and median N_p. The WSA-Enlil model, regardless of synoptic map input, tends to overrate the slow wind speed and underestimate maximum N_p, B, and T_p substantially.

The CCMC models often match with time series of normalized parameters and the timing of SBs and SIs better than the persistence models using the in situ observations taken 2–4 days ahead. The 1 and 27 day persistence models perform well, but the former has very short warning time and the latter greatly benefits from the quasi-steady solar wind and recurrent SIRs in the late declining phase. They would meet greater challenges when the Sun is more active, which will be tested in the future study. Nevertheless, the CCMC models are vital to provide the solar wind condition in the vast space where the continuous solar wind monitoring is often missing.

From the composite rankings of capturing time series of normalized solar wind parameters (Figure 7), SBs (Figure 15f), and SIRs (Figure 17e), the GONG-WSA-Enlil model is a sensible choice for space weather operation. However, as summarized in Table 1, each model has its own strengths and weaknesses. We cannot simply say one model is superior to another. All of the models make different simplifying assumptions, treating the physics in very approximate fashion in many aspects; thus, the model performance is also a test of how well those assumptions can simulate the nature. The difference in performance may be largely attributed to how different models handle the input data, rather than the physics behind the models. For example, the SWMF v9.20 with more physics involved and starting from the top of chromosphere cannot perform as well as v8.03. The paradigm could be shifted in a newer version. This also demonstrates that model performance can be changed greatly with model upgrades, and a newer version does not necessarily work better and needs persistent validation.

From the study, we have also learned that we cannot over interpret the comparison results using the quantitative metric such as MSE or the statistics of parameters. For instance, the SWMF v9.20 has lower MSE and better match with the statistics of solar wind parameters than some other models in Figures 6, 7, and 12, but from the visual inspections in Figures 2–5, SWMF v9.20 clearly mismatches with the solar wind patterns most. The GONG-MAS v4.7 Polytropic-Enlil model has the highest correlation coefficient for *B*, but it has larger MSE for *B* and normalized *B* than many other models. Thus, we need to validate models comprehensively, both qualitatively and quantitatively. In addition, the dramatic differences in Figures 6 and 7 demonstrate that it is necessary to separate the discrepancy brought by the misestimation of average values when comparing MSE. For example, the GONG-WSA-Enlil model matches with time series of *B* worst but matches with time series of normalized *B* best.

In the past, *Owens et al*. [2008], *Riley et al*. [2011], and other studies found that the empirically based solutions tended to match with in situ observations better. With the improvement of the physics used in the models and better constraining of free parameters, now in this validation we see that the self-consistently derived models can perform better in many aspects than the empirical models using the same synoptic map as input. We expect that the advantages of the physics-based models will be more evident in the future.

With the growth of computer-processing power, the high-resolution photospheric observations from the Helioseismic and Magnetic Imager on board the Solar Dynamics Observatory, the refinement of ADAPT model and the magnetogram interpolation and composition tool, as well as the unprecedented observations from the upcoming Solar Orbiter and Solar Probe Plus missions flying much closer to the Sun, the coronal and heliospheric models will be advanced significantly in the near future. Systematic validation will continuously be one vital contributor to such model development and to facilitate its application in scientific research and space weather operations. Meanwhile, we will learn more about the missing physics by developing and applying these models.

Acknowledgments

This work is supported by NSF grants AGS 1242798, 1321493 and 1259549. A.T. and I.V.S. are supported by NSF grant AGS 1257519. Simulation results have been provided by the CCMC at NASA/GSFC through their public Runs on Request system (http://ccmc.gsfc.nasa.gov/requests/requests.php). The results of IPS tomography are available upon request from Bernard Jackson at UCSD. The simulation results of other models are available to the public at http://ccmc.gsfc.nasa.gov/ungrouped/SH/Helio_main.php by searching "Jian" as run requestor's last name and choosing 2056–2062 as the Carrington rotation number. The CCMC is a multiagency partnership between NASA, AFMC, AFOSR, AFRL, AFWA, NOAA, NSF, and ONR. We are grateful to the CCMC team for their work. We thank the GONG, SOHO/MDI, MWO, and NSO teams for providing the photospheric magnetograms. We appreciate Nick Arge for providing the WSA coronal model at the CCMC and thank all the other modeling teams (see section 2) for providing their models at the CCMC and for their consultation. We acknowledge the Space Physics Data Facility at NASA/GSFC for providing OMNI data (see http://omniweb.gsfc.nasa.gov/). L.K.J. thanks Janet Luhmann and Christopher Russell for helpful discussion.

References

Altschuler, M. A., and G. Newkirk Jr. (1969), Magnetic fields and the structure of the solar corona, *Sol. Phys.*, *9*, 131–149, doi:10.1007/BF00145734.

Anderson, R. L., G. H. Born, and J. M. Forbes (2009), Sensitivity of orbit predictions to density variability, *J. Spacecr. Rockets*, *46*, 1214–1230, doi:10.2514/1.42138.

Arge, C. N., and V. J. Pizzo (2000), Improvement in the prediction of solar wind conditions using real-time solar magnetic field updates, *J. Geophys. Res.*, *105*, 10,465–10,479, doi:10.1029/1999JA000262.

Arge, C. N., D. Odstrcil, V. J. Pizzo, and L. Mayer (2002), Improved method for specifying solar wind speed near the Sun, in *Solar Wind Ten, AIP Conf. Proc*, vol. 679, edited by M. Velli and R. Bruno, pp. 190–193, AIP, Melville, New York, doi:10.1063/1.1618574.

Arge, C. N., C. J. Henney, J. Koller, C. R. Compeau, S. Young, D. MacKenzie, A. Fay, and J. W. Harvey (2010), Air Force Data Assimilative Photospheric Flux Transport (ADAPT) model, in *Solar Wind 12, AIP Conf. Proc*, vol. 1216, edited by M. Maksimovic et al., pp. 343–346, AIP, Melville, New York, doi:10.1063/1.3395870.

Arge, C. N., C. J. Henney, J. Koller, W. A. Toussaint, J. W. Harvey, and S. Young (2011), Improving data drivers for coronal and solar wind models, in *5th International Conference of Numerical Modeling of Space Plasma Flows: ASTRONUM-2010, ASP Conf. Ser*, vol. 444, edited by N. V. Pogorelov, E. Audit, and G. P. Zank, pp. 99–104, ASP, San Francisco, Calif.

Arge, C. N., C. J. Henney, I. G. Hernandez, W. A. Toussaint, J. Koller, and H. C. Godinez (2013), Modeling the corona and solar wind using ADAPT maps that include far-side observations, in *Solar Wind 13, AIP Conf. Proc*, vol. 1539, edited by G. P. Zank et al., pp. 11–14, AIP, Melville, New York, doi:10.1063/1.4810977.

Belcher, J. W., and L. Davis Jr. (1971), Large-amplitude Alfvén waves in the interplanetary medium, 2, *J. Geophys. Res.*, *76*, 3534–3563, doi:10.1029/JA076i016p03534.

Brecht, S. H., J. Lyon, J. A. Fedder, and K. Hain (1981), A simulation study of east–west IMF effects on the magnetosphere, *Geophys. Res. Lett.*, *8*, 397–400, doi:10.1029/GL008i004p00397.

Case, A. W., H. E. Spence, M. J. Owens, P. Riley, and D. Odstrcil (2008), Ambient solar wind's effect on ICME transit time, *Geophys. Res. Lett.*, *35*, L15105, doi:10.1029/2008GL034493.
Chen, G.-M., J. Xu, W. Wang, and A. G. Burns (2014), A comparison of the effects of CIR- and CME-induced geomagnetic activity on thermospheric densities and spacecraft orbits: Statistical studies, *J. Geophys. Res. Space Physics*, *119*, 7928–7939, doi:10.1002/2014JA019831.
Colaninno, R. C., A. Vourlidas, and C. C. Wu (2013), Quantitative comparison of methods for predicting the arrival of coronal mass ejections at Earth based on multiview imaging, *J. Geophys. Res. Space Physics*, *118*, 6866–6879, doi:10.1002/2013JA019205.
Coles, W. A. (1978), Interplanetary scintillation, *Space Sci. Rev.*, *21*, 411–425, doi:10.1007/BF00173067.
Collinson, G. A., et al. (2015), The Impact of a Slow Interplanetary Coronal Mass Ejection (ICME) on Venus, *J. Geophys. Res. Space Physics*, doi:10.1002/2014JA020616, in press.
Crooker, N. U., J. T. Gosling, and S. W. Kahler (1998), Magnetic clouds at sector boundaries, *J. Geophys. Res.*, *103*, 301–306, doi:10.1029/97JA02774.
Eyles, C. J., G. M. Simnett, M. P. Cooke, B. V. Jackson, A. Buffington, P. P. Hick, N. R. Waltham, J. M. King, P. A. Anderson, and P. E. Holladay (2003), The Solar Mass Ejection Imager (SMEI), *Sol. Phys.*, *217*, 319–347, doi:10.1023/B:SOLA.0000006903.75671.49.
Fedder, J. A., J. G. Lyon, S. P. Slinker, and C. M. Mobarry (1995), Topological structure of the magnetotail as a function of interplanetary magnetic field direction, *J. Geophys. Res.*, *100*, 3613–3621, doi:10.1029/94JA02577.
Gombosi, T. I., D. L. De Zeeuw, C. P. T. Groth, K. G. Powell, C. R. Clauer, and P. Song (2001), From Sun to Earth: Multiscale MHD simulations of space weather, in *Space Weather, Geophys. Monogr. Ser*, vol. 125, edited by P. Song, H. J. Singer, and G. L. Siscoe, pp. 169–176, AGU, Washington, D. C., doi:10.1029/GM125p0169.
Gombosi, T. I., et al. (2004), Solution-adaptive magnetohydrodynamics for space plasmas: Sun-to-Earth simulations, *Comput. Sci. Eng.*, *6*, 14–35, doi:10.1109/MCISE.2004.1267603.
Gonzalez, W. D., J. A. Joselyn, Y. Kamide, H. W. Kroehl, G. Rostoker, B. T. Tsurutani, and V. M. Vasyliunas (1994), What is a geomagnetic storm?, *J. Geophys. Res.*, *99*, 5771–5792, doi:10.1029/93JA02867.
González-Esparza, J. A., A. Carrillo, E. Andrade, P. Sierra, S. Vazquez, C. Rodríguez, R. Pérez-Enríquez, S. Kurtz, and X. Blanco-Cano (2006), Calibration and testing of the MEXART antenna using solar transients, *Adv. Space Res.*, *38*, 1824–1827, doi:10.1016/j.asr.2005.09.032.
Gopalswamy, N., P. Mäkelä, H. Xie, S. Akiyama, and S. Yashiro (2009), CME interactions with coronal holes and their interplanetary consequences, *J. Geophys. Res.*, *114*, A00A22, doi:10.1029/2008JA013686.
Gosling, J. T., and V. J. Pizzo (1999), Formation and evolution of corotating interaction regions and their three dimensional structure, *Space Sci. Rev.*, *89*, 21–52, doi:10.1023/A:1005291711900.
Harvey, J. W., et al. (1996), The Global Oscillation Network Group (GONG) project, *Science*, *272*, 1284–1286, doi:10.1126/science.272.5266.1284.
Heppner, J. P. (1972), Polar-cap electric field distributions related to the interplanetary magnetic field direction, *J. Geophys. Res.*, *77*, 4877–4887, doi:10.1029/JA077i025p04877.
Hewish, A., P. F. Scott, and D. Wills (1964), Interplanetary scintillation of small diameter radio sources, *Nature*, *203*, 1214–1217, doi:10.1038/2031214a0.
Hundhausen, A. J. (1993), Sizes and locations of coronal mass ejections: SMM observations from 1980 and 1984–1989, *J. Geophys. Res.*, *98*, 13,177–13,200, doi:10.1029/93JA00157.
Jackson, B. V., P. L. Hick, M. Kojima, and A. Yokobe (1997), Heliospheric tomography using interplanetary scintillation observations, *Phys. Chem. Earth*, *22*, 425–434, doi:10.1016/S0079-1946(97)00170-5.
Jackson, B. V., P. L. Hick, M. Kojima, and A. Yokobe (1998), Heliospheric tomography using interplanetary scintillation observations: 1. Combined Nagoya and Cambridge data, *J. Geophys. Res.*, *103*, 12,049–12,067, doi:10.1029/97JA02528.
Jackson, B. V., et al. (2004), The Solar Mass-Ejection Imager (SMEI) mission, *Sol. Phys.*, *225*, 177–207, doi:10.1007/s11207-004-2766-3.
Jackson, B. V., P. P. Hick, A. Buffington, M. M. Bisi, J. M. Clover, M. Tokumaru, M. Kojima, and K. Fujiki (2011), Three-dimensional reconstruction of heliospheric structure using iterative tomography: A review, *J. Atoms. Sol. Terr. Phys.*, *73*, 1214–1227, doi:10.1016/j.jastp.2010.10.007.
Jackson, B. V., et al. (2015), The UCSD kinematic IPS solar wind boundary and its use in the ENLIL 3-D MHD prediction model, *Space Weather*, *13*, 104–115, doi:10.1002/2014SW001130.
Jian, L., C. T. Russell, J. G. Luhmann, and R. M. Skoug (2006), Properties of stream interactions at one AU during 1995–2004, *Sol. Phys.*, *239*, 337–392, doi:10.1007/s11207-006-0132-3.
Jian, L. K., C. T. Russell, and J. G. Luhmann (2011a), Comparing solar minimum 23/24 with historical solar wind records at 1 AU, *Sol. Phys.*, *274*, 321–344, doi:10.1007/s11207-011-9737-2.
Jian, L. K., C. T. Russell, J. G. Luhmann, P. J. MacNeice, D. Odstrcil, P. Riley, J. A. Linker, R. M. Skoug, and J. T. Steinberg (2011b), Comparison of observations at ACE and Ulysses with Enlil model results: Stream interaction regions during Carrington rotations 2016–2018, *Sol. Phys.*, *273*, 179–203, doi:10.1007/s11207-011-9858-7.
King, J. H., and N. E. Papitashvili (2005), Solar wind spatial scales in and comparison of hourly Wind and ACE plasma and magnetic field data, *J. Geophys. Res.*, *110*, A02104, doi:10.1029/2004JA010649.
Lee, C. O., J. G. Luhmann, D. Odstrcil, P. J. MacNeice, I. de Pater, P. Riley, and C. N. Arge (2009), The solar wind at 1 AU during the declining phase of solar cycle 23: Comparison of 3D numerical model results with observations, *Sol. Phys.*, *254*, 155–183, doi:10.1007/s11207-008-9280-y.
Lee, C. O., J. G. Luhmann, J. T. Hoeksema, X. Sun, C. N. Arge, and I. de Pater (2011), Coronal field opens at lower height during the solar cycles 22 and 23 minimum periods: IMF comparison suggests the source surface should be lowered, *Sol. Phys.*, *269*, 367–388, doi:10.1007/s11207-010-9699-9.
Linker, J. A., Z. Mikić, and D. D. Schnack (1996), Global coronal modeling and space weather prediction, in *Solar Drivers of Interplanetary and Terrestrial Disturbances, ASP Conf. Ser*, vol. 95, edited by K. S. Balasubramaniam, S. L. Keil, and R. N. Smartt, pp. 208–218, ASP, San Francisco, Calif.
Linker, J. A., Z. Mikić, R. Lionello, P. Riley, T. Amari, and D. Odstrcil (2003), Flux cancellation and coronal mass ejections, *Phys. Plasmas*, *10*, 1971–1978, doi:10.1063/1.1563668.
Lionello, R., J. A. Linker, and Z. Mikić (2009), Multispectral emission of the Sun during the first whole Sun month: Magnetohydrodynamic simulations, *Astrophys. J.*, *690*, 902–912, doi:10.1088/0004-637X/690/1/902.
Lopez, R. E. (1987), Solar-cycle invariance in the solar wind proton temperature relationships, *J. Geophys. Res.*, *92*, 11,189–11,194, doi:10.1029/JA092iA10p11189.
MacNeice, P. (2009a), Validation of community models: Identifying events in space weather model timelines, *Space Weather*, *7*, S06004, doi:10.1029/2009SW000463.
MacNeice, P. (2009b), Validation of community models: 2 Development of a baseline using the Wang-Sheeley-Arge model, *Space Weather*, *7*, S12002, doi:10.1029/2009SW000489.
Manchester, W. B., J. U. Kozyra, S. T. Lepri, and B. Lavraud (2014), Simulation of magnetic cloud erosion during propagation, *J. Geophys. Res. Space Physics*, *119*, 5499–5464, doi:10.1002/2014JA019882.

Manoharan, P. K. (2010), Ooty interplanetary scintillation—Remote-sensing observations and analysis of coronal mass ejections in the heliosphere, *Sol. Phys.*, *265*, 137–157, doi:10.1007/s11207-010-9593-5.
Manoharan, P. K., S. Ananthakrishnan, M. Dryer, T. R. Detman, H. Leinbach, M. Kojima, T. Watanabe, and J. Kahn (1995), Solar wind velocity and normalized scintillation index from single-station IPS observations, *Sol. Phys.*, *156*, 377–393, doi:10.1007/BF00670233.
Mays, M. L., et al. (2015), Ensemble modeling of CMEs using the WSA-ENLIL+Cone model, *Sol. Phys.*, doi:10.1007/s11207-015-0692-1, in press.
Mikić, Z., and J. A. Linker (1994), Disruption of coronal magnetic field arcades, *Astrophys. J.*, *430*, 898–912, doi:10.1086/174460.
Mikić, Z., and J. A. Linker (1996), The large-scale structure of the solar corona and inner heliosphere, in *Solar Wind Eight, AIP Conf. Proc*, vol. 382, edited by D. Winterhalter, et al., pp. 104–107, AIP, Woodbury, NY, doi:10.1063/1.51370.
Millward, G., D. Biesecker, V. Pizzo, and C. A. Koning (2013), An operational software tool for the analysis of coronagraph images: Determining CME parameters for input into the WSA-Enlil heliospheric model, *Space Weather*, *11*, 57–68, doi:10.1002/swe.20024.
Miyoshi, Y., and R. Kataoka (2005), Ring current ions and radiation belt electrons during geomagnetic storms driven by coronal mass ejections and corotating interaction regions, *Geophys. Res. Lett.*, *32*, L21105, doi:10.1029/2005GL024590.
Odstrčil, D. (1994), Interaction of solar wind streams and related small structures, *J. Geophys. Res.*, *99*, 17,653–17,671, doi:10.1029/94JA01225.
Odstrcil, D. (2003), Modeling 3-D solar wind structure, *Adv. Space Res.*, *32*, 497–506, doi:10.1016/S0273-1177(03)00332-6.
Odstrčil, D., and V. J. Pizzo (1999a), Three-dimensional propagation of coronal mass ejections (CMEs) in a structured solar wind flow: 1. CME launched within the streamer belt, *J. Geophys. Res.*, *104*, 483–492, doi:10.1029/1998JA900019.
Odstrčil, D., and V. J. Pizzo (1999b), Three-dimensional propagation of coronal mass ejections (CMEs) in a structured solar wind flow: 2. CME launched adjacent to the streamer belt, *J. Geophys. Res.*, *104*, 493–503, doi:10.1029/1998JA900038.
Odstrčil, D., M. Dryer, and Z. Smith (1996), Propagation of an interplanetary shock along the heliospheric plasma sheet, *J. Geophys. Res.*, *101*, 19,973–19,986, doi:10.1029/96JA00479.
Odstrcil, D., J. A. Linker, R. Lionello, Z. Mikić, P. Riley, V. J. Pizzo, and J. G. Luhmann (2002), Merging of coronal and heliospheric numerical two dimensional MHD models, *J. Geophys. Res.*, *107*, 1493, doi:10.1029/2002JA009334.
Odstrcil, D., V. J. Pizzo, J. A. Linker, P. Riley, R. Lionello, and Z. Mikić (2004), Initial coupling of coronal and heliospheric numerical magnetohydrodynamic codes, *J. Atoms. Sol. Terr. Phys.*, *66*, 1311–1320, doi:10.1016/j.jastp.2004.04.007.
Owens, M. J., C. N. Arge, H. E. Spence, and A. Pembroke (2005), An event-based approach to validating solar wind speed predictions: High-speed enhancements in the Wang-Sheeley-Arge model, *J. Geophys. Res.*, *110*, A12105, doi:10.1029/2005JA011343.
Owens, M. J., H. E. Spence, S. McGregor, W. J. Hughes, J. M. Quinn, C. N. Arge, P. Riley, J. Linker, and D. Odstrcil (2008), Metrics for solar wind prediction models: Comparison of empirical, hybrid, and physics-based schemes with 8 years of L1 observations, *Space Weather*, *6*, S08001, doi:10.1029/2007SW000380.
Pierce, A. K. (1969), The solar program of the Kitt peak national observatory, *Sol. Phys.*, *6*, 498–503, doi:10.1007/BF00146486.
Pizzo, V., G. Millward, A. Parsons, D. Biesecker, S. Hill, and D. Odstrcil (2011), Wang-Sheeley-Arge-Enlil Cone model transitions to operations, *Space Weather*, *9*, S03004, doi:10.1029/2011SW000663.
Poduval, B., and X. P. Zhao (2014), Validating solar wind prediction using the current sheet source surface model, *Astrophys. J. Lett.*, *782*, L22.
Powell, K. G., P. L. Roe, T. J. Linde, T. I. Gombosi, and D. L. De Zeeuw (1999), A solution-adaptive upwind scheme for ideal magnetohydrodynamics, *J. Comput. Phys.*, *154*, 284–309, doi:10.1006/jcph.1999.6299.
Riley, P., J. A. Linker, and Z. Mikić (2001a), An empirically-driven global MHD model of the solar corona and inner heliosphere, *J. Geophys. Res.*, *106*, 15,889–15,901, doi:10.1029/2000JA000121.
Riley, P., J. A. Linker, Z. Mikić, and R. Lionello (2001b), MHD modeling of the solar corona and inner heliosphere: Comparison with observations, in *Space Weather, Geophys. Monogr. Ser*, vol. 125, edited by P. Song, H. J. Singer, and G. L. Siscoe, pp. 159–167, AGU, Washington, D.C., doi:10.1029/GM125p0159.
Riley, P., J. A. Linker, Z. Mikić, D. Odstrcil, and V. J. Pizzo (2002), Evidence of posteruption reconnection associated with coronal mass ejections in the solar wind, *Astrophys. J.*, *578*, 972–978, doi:10.1086/342608.
Riley, P., R. Lionello, J. A. Linker, Z. Mikić, J. Luhmann, and J. Wijaya (2011), Global MHD modeling of the solar corona and inner heliosphere for the whole heliosphere interval, *Sol. Phys.*, *274*, 361–377, doi:10.1007/s11207-010-9698-x.
Russell, C. T., and R. L. McPherron (1973), The magnetotail and substorms, *Space Sci. Rev.*, *15*, 205–266, doi:10.1007/BF00169321.
Schatten, K. H. (1971), Current sheet magnetic model for the solar corona, *Cosmic Electrodyn.*, *2*, 232–245.
Schatten, K. H., J. M. Wilcox, and N. F. Ness (1969), A model of interplanetary and coronal magnetic fields, *Sol. Phys.*, *6*, 442–455, doi:10.1007/BF00146478.
Scherrer, P. H., et al. (1995), The solar oscillation investigation—Michelson Doppler imager, *Sol. Phys.*, *162*, 129–188, doi:10.1007/BF00733429.
Smith, E. J., and J. H. Wolfe (1976), Observations of interaction regions and corotating shocks between one and five AU: Pioneers 10 and 11, *Geophys. Res. Lett.*, *3*, 137–140, doi:10.1029/GL003i003p00137.
Sokolov, I. V., B. van der Holst, R. Oran, C. Downs, I. Roussev, M. Jin, W. B. Manchester IV, R. M. Evans, and T. I. Gombosi (2013), Magnetohydrodynamic waves and coronal heating: Unifying empirical and MHD turbulence models, *Astrophys. J.*, *764*, 23, doi:10.1088/0004-637X/764/1/23.
Swarup, G., N. V. G. Sarma, M. N. Joshi, V. K. Kapahi, D. S. Bagri, S. H. Damle, S. Ananthakrishnan, V. Balasubramanian, S. S. Bhave, and R. P. Sinha (1971), Large steerable radio telescope at Ootacamund, India, *Nat. Phys. Sci.*, *230*, 185–188, doi:10.1038/physci230185a0.
Tokumaru, M. (2013), Three-dimensional exploration of the solar wind using observations of interplanetary scintillation, *Proc. Jpn. Acad. Ser. B*, *89*, 67–79, doi:10.2183/pjab.89.67.
Tokumaru, M., M. Kojima, K. Fujiki, K. Maruyama, Y. Maruyama, H. Ito, and T. Iju (2011), A newly developed UHF radiotelescope for interplanetary scintillation observations: Solar Wind Imaging Facility, *Radio Sci.*, *46*, RS0F02, doi:10.1029/2011RS004694.
Tóth, G., et al. (2005), Space weather modeling framework: A new tool for the space science community, *J. Geophys. Res.*, *110*, A12226, doi:10.1029/2005JA011126.
Tóth, G., et al. (2012), Adaptive numerical algorithms in space weather modeling, *J. Comput. Phys.*, *231*, 870–903, doi:10.1016/j.jcp.2011.02.006.
Ulrich, R. K., S. Evans, J. E. Boyden, and L. Webster (2002), Mount Wilson synoptic magnetic fields: Improved instrumentation, calibration, and analysis applied to the 14 July 2000 flare and to the evolution of the dipole field, *Astrophys. J. Suppl.*, *139*, 259–279, doi:10.1086/337948.
van der Holst, B., W. B. Manchester IV, R. A. Frazin, A. M. Vásquez, G. Tóth, and T. I. Gombosi (2010), A data-driven, two-temperature solar wind model with Alfvén waves, *Astrophys. J.*, *725*, 1373–1383, doi:10.1088/0004-637X/725/1/1373.
van der Holst, B., I. V. Sokolov, X. Meng, M. Jin, W. B. Manchester IV, G. Tóth, and T. I. Gombosi (2014), Alfvén Wave Solar Model (AWSoM): Coronal heating, *Astrophys. J.*, *782*, 81, doi:10.1088/0004-637X/782/2/81.
van Haarlem, M. P., et al. (2013), LOFAR: The low-frequency array, *Astron. Astrophys.*, *556*, 53, doi:10.1051/0004-6361/201220873.
Vandas, M., and D. Odstrčil (2000), Magnetic cloud evolution: A comparison of analytical and numerical solutions, *J. Geophys. Res.*, *105*, 12,605–12,616, doi:10.1029/2000JA900027.

Vršnak, B., M. Temmer, T. Žic, A. Taktakishvili, M. Dumbović, C. Möstl, A. M. Veronig, M. L. Mays, and D. Odstrčil (2014), Heliospheric propagation of coronal mass ejections: Comparison of numerical WSA-ENLIL+Cone model and analytical drag-based model, *Astrophys. J. Supp.*, *213*, 21, doi:10.1088/0067-0049/213/2/21.

Wang, Y. M., and N. R. Sheeley Jr. (1990a), Solar wind speed and coronal flux-tube expansion, *Astrophys. J.*, *355*, 726–732, doi:10.1086/168805.

Wang, Y. M., and N. R. Sheeley Jr. (1990b), Magnetic flux transport and the sunspot-cycle evolution of coronal holes and their wind streams, *Astrophys. J.*, *365*, 372–386, doi:10.1086/169492.

Wang, Y. M., and N. R. Sheeley Jr. (1992), On potential field models of the solar corona, *Astrophys. J.*, *392*, 310–319, doi:10.1086/171430.

Wilson, G. R., D. R. Weimer, J. O. Wise, and F. A. Marcos (2006), Response of the thermosphere to Joule heating and particle precipitation, *J. Geophys. Res.*, *111*, A10314, doi:10.1029/2005JA011274.

Xu, J., W. Wang, J. Lei, E. K. Sutton, and G. Chen (2011), The effect of periodic variations of thermospheric density on CHAMP and GRACE orbits, *J. Geophys. Res.*, *116*, A02315, doi:10.1029/2010JA015995.

Zhang, X.-Y., and M. B. Moldwin (2014), The source, statistical properties, and geoeffectiveness of long-duration southward interplanetary magnetic field intervals, *J. Geophys. Res. Space Physics*, *119*, 658–669, doi:10.1002/2013JA018937.

Zhao, X., and J. T. Hoeksema (1995), Prediction of the interplanetary magnetic field strength, *J. Geophys. Res.*, *100*, 19–33, doi:10.1029/94JA02266.

Zheng, Y., et al. (2013), Forecasting propagation and evolution of CMEs in an operational setting: What has been learned, *Space Weather*, *11*, 1–18, doi:10.1002/swe.20096.